2	Early Eocene ocean meridional overturning circulation: the roles of atmospheric forcing and strait geometry
4	
5 6 7 8 9	Yurui Zhang <sup>1*</sup> , Agatha M. de Boer <sup>2</sup> , Daniel J. Lunt <sup>3</sup> , David K. Hutchinson <sup>2,4</sup> , Phoebe Ross <sup>5</sup> , Tina van de Flierdt <sup>5</sup> , Philip Sexton <sup>6</sup> , Helen K. Coxall <sup>2</sup> , Sebastian Steinig <sup>3</sup> , Jean-Baptiste Ladant <sup>7</sup> , Jiang Zhu <sup>8</sup> , Yannick Donnadieu <sup>9</sup> , Zhongshi Zhang <sup>10</sup> , Wing-Le Chan <sup>11</sup> , Ayako Abe-Ouchi <sup>11</sup> , Igor Niezgodzki <sup>12,13</sup> , Gerrit Lohmann <sup>12</sup> , Gregor Knorr <sup>12</sup> , Christopher J. Poulsen <sup>14</sup> , Matt Huber <sup>15</sup>
10	
11 12	<sup>1</sup> State Key Laboratory of Marine Environmental Science, College of Ocean & Earth Sciences, Xiamen University, Xiamen, China
13 14	<sup>2</sup> Department of Geological Sciences, Bolin Centre for Climate Research, Stockholm University, Sweden
15	<sup>3</sup> School of Geographical Sciences, University of Bristol, UK
16	<sup>4</sup> Climate Change Research Centre, University of New South Wales, Sydney, Australia
17 18	<sup>5</sup> Department of Earth Science and Engineering, Imperial College London, South Kensington Campus, London, UK
19	<sup>6</sup> School of Environment, Earth and Ecosystem Sciences, The Open University, UK
20 21	<sup>7</sup> Laboratoire des Sciences du Climat et de l'Environnement, LSCE/IPSL, UMR 8212, CEA-CNRS-UVSQ, Université Paris-Saclay, France
22 23	<sup>8</sup> Climate and Global Dynamics Laboratory, National Center for Atmospheric Research, Boulder, Colorado, USA.
24	<sup>9</sup> Aix Marseille Univ, CNRS, IRD, INRA, Coll France, CEREGE, Aix-en-Provence, France
25	<sup>10</sup> Department of Atmosphere Science, China University of Geoscience, Wuhan, China
26	<sup>11</sup> AORI, The University of Tokyo, Kashiwa, Japan
27 28	<sup>12</sup> Alfred Wegener Institute, Helmholtz Centre for Polar and Marine Research, Bremerhaven, Germany
29 30	<sup>13</sup> INGPAN – Institute of Geological Sciences, Polish Academy of Sciences, Research Center in Kraków, Kraków, Poland

<sup>14</sup>Department of Earth and Environmental Sciences, University of Michigan, Ann Arbor, 31 Michigan, USA 32 <sup>15</sup>Department of Earth, Atmospheric, and Planetary Sciences, Purdue University, USA 33 34 Corresponding author: first and last name (yuruizhang@xmu.edu.cn) 35 36 **Key Points:** 37 This study evaluates the ocean's meridional overturning circulation during the early 38 Eocene in eight models of the DeepMIP project 39 The primary region of deep-water formation depends both on the atmospheric freshwater 40 flux and the strait geometry in the Southern Ocean 41 Compatible with proxy records, six of eight models show that deep waters predominantly 42 originated from the south 43 44 45

#### Abstract

46

47

48

49

50

51

52

53

54

55

56

57

58

59

60

61

62

63

64

65

66

67

68

69

Here, we compare the ocean overturning circulation of the early Eocene (47-56 Ma) in eight coupled climate model simulations from the Deep-Time Model Intercomparison Project (DeepMIP), and investigate the causes of the observed inter-model spread. The most common global meridional overturning circulation (MOC) feature of these simulations is the anticlockwise bottom cell, fed by sinking in the Southern Ocean. In the North Pacific, one model (GFDL) displays strong deepwater formation and one model (CESM) shows weak deepwater formation, while in the Atlantic two models show signs of weak intermediate water formation (MIROC and NorESM). The location of the Southern Ocean deepwater formation sites varies among models and relates to small differences in model geometry of the Southern Ocean gateways. Globally, convection occurs in the basins with smallest local freshwater gain from the atmosphere. The global MOC is insensitive to atmospheric CO<sub>2</sub> concentrations from 1x (i.e. 280 ppm) to 3x (840ppm) pre-industrial levels. Only two models have simulations with higher CO<sub>2</sub> (i.e. CESM and GFDL) and these show divergent responses, with a collapsed and active MOC, respectively, possibly due to differences in spin-up conditions. Combining the multiple model results with available proxy data on abyssal ocean circulation highlights that strong Southern Hemisphere-driven overturning is the most likely feature of the early Eocene. In the North Atlantic, unlike the present day, neither model results nor proxy data suggest deepwater formation in the open ocean during the early Eocene, while the evidence for deepwater formation in the North Pacific remains inconclusive.

#### Plain language summary

The ocean's overturning circulation refers to the replenishment of the ocean's deep water by cold dense polar surface waters and its eventual return to the surface. It affects the climate through redistribution of heat across the globe and uptake of atmosphere carbon dioxide (CO<sub>2</sub>). Here, we

explore the overturning circulation of the Early Eocene, a hot period 47-56 million years ago when atmosphere CO<sub>2</sub> levels were similar to the "worst case" projections for the end of this century, in eight climate models setup up for that time. Our results, together with available ocean circulation sediment data for the time, indicate that during the early Eocene deep water originated predominantly from cold surface waters around Antarctica. The North Atlantic source of deep water that today contributes to European's relatively mild climate for its latitude, was completely absent at the time. Interestingly, even when the carbon dioxide in the Eocene model simulations were lowered to levels similar to today and before the industrial revolution, the North Atlantic source of deep water remains absent, indicating that it is the distribution of continents and ice-sheets, rather than CO<sub>2</sub> that is responsible for the difference between the modern and Eocene circulation.

#### 1 Introduction

Large-scale ocean circulation is an important component of the Earth's climate and is coupled with geochemical and biogeochemical processes in the ocean. As a key element of ocean circulation, the global meridional overturning circulation (MOC) affects the global climate by redistributing heat and influencing air-sea interactions (e.g. Msadek et al., 2013; Rose & Ferreira, 2013; Trenberth & Caron, 2001). MOC facilitates poleward meridional heat transport (e.g. up to 1.3 PW in the North Atlantic at 26.5°N; Johns et al., 2011), making polar regions warmer than they would be otherwise. Over geological time, the variation in ocean circulation intertwines with the evolution of Earth's climate system through direct and indirect processes (e.g. as summarized in Ferreira et al., 2018). As an example of direct processes, a changing MOC perturbs the pattern of heat transport, which in turn modifies large-scale climate features. Different MOC modes in the abyss can also indirectly influence the Earth system by partitioning carbon between different reservoirs through a multitude of geochemical and biogeochemical

processes (e.g. Elsworth et al., 2017). For instance, dust-borne iron fertilization interacting with weakened Southern Ocean overturning has been proposed as the main cause of atmospheric CO<sub>2</sub> drawdown during the latter stages of Pleistocene glacial periods (Chalk et al., 2017).

Although the geological past is an imperfect analogue for the present and future, it remains the unique avenue for understanding large-scale Earth system behavior and sensitivity under changing climate states (Sherwood et al., 2020; Tierney et al., 2020). Across the spectrum of different climate states (Hothouse, Warmhouse, Coolhouse, Icehouse) during the past 66 million years (Westerhold et al., 2020), the early Eocene (47-56 million years ago) was the last Hothouse interval (Bijl et al., 2009; Cramer et al., 2011; Cramwinckel et al., 2018; Harrington et al., 2012; Hollis et al., 2009; Markwick, 1998; Pross et al., 2012; Utescher & Mosbrugger, 2007). The Eocene thus offers a valuable opportunity to explore the response of ocean circulation under acute warmth, when higher temperatures led to enhanced global hydrological cycle and flattened latitudinal temperature gradients that had a stronger impact on density gradients (via the non-linear equation of state), and thus stratification and convection (e.g. de Boer et al., 2007).

The question of the operation and geometry of the global MOC during the early Eocene is of great interest given the analogous hothouse climate of current global change. The paleogeography had a near modern-day configuration by the early Eocene particularly with respect to polar continental distribution, with Antarctica sitting centrally over the southern pole, and continent circling the Arctic Ocean at the North Pole. There were however, significant differences with respect to tectonically active regions. For example, in the early Eocene, the Tibetan plateau was much lower than today, whereas the Rocky Mountains had almost reached their present day height (Herold et al., 2014). At low latitudes, open Panama and Tethys Seaways provided tropical ocean connections. In the Southern Hemisphere, closed or very narrow Drake Passage and Tasman Seaway connections separated different parts of the Southern Ocean from each other, although much uncertainty remains in the precise chronology of widening and deepening (Tournoulin et al. 2021: Bijl et al., 2013). At high northern latitudes the Arctic Ocean was only

barely connected to the North Atlantic and was isolated from the Pacific Ocean (O'Regan et al., 2011). The effects of Eocene paleogeography on ocean circulation and climate have been widely investigated (Baatsen et al., 2020; Huber & Sloan, 2001; Hutchinson et al., 2019; Nong et al., 2000). Studies specifically exploring the effects of ocean gateways suggest that the opening of key gateways in both hemispheres may cause significant re-organization of the ocean circulation in climate models under Eocene condition (England et al., 2017; Nong et al., 2000; Roberts et al., 2009; Toggweiler & Bjornsson, 2000). Furthermore, the interplay of different gateways' effects on ocean circulation may have been significant (Ladant et al., 2018; Yang et al., 2014). For example, Yang et al. (2014) found that closing the Drake Passage tends to suppress North Atlantic deep water sinking and promote the emergence of a strong Southern Ocean overturning circulation, only when the Panama Seaway is open, such as during the Eocene; whereas the Atlantic MOC may remain intense when the Panama Seaway is closed.

Given a much higher but uncertain atmospheric CO<sub>2</sub> during the Eocene (e.g. Anagnostou et al., 2020; Foster et al., 2017), several paleoclimate studies have explored the global MOC responses to changing atmospheric CO<sub>2</sub> concentrations in climate models ranging from idealized to coupled models. However, there is no consensus on the global MOC response among these studies yet, because modelling results suggest diverse responses depending on the model used (e.g. Hutchinson et al., 2018; Lunt et al., 2010; Monteiro et al., 2012). On the one hand, MOC strength weakens under high CO<sub>2</sub> conditions in some models (Hutchinson et al., 2018; Lunt et al., 2010). On the other hand, Monteiro et al. (2012) simulated an increased MOC with elevated CO<sub>2</sub> concentrations using the GENIE model, and Thomas et al. (2014), Winguth et al. (2012) and Donnadieu et al. (2016) found insensitive MOC responses. Several factors, such as different simulation setups and durations, may partially explain these discrepancies, as discussed in Zhang et al. (2020). The divergent responses are also likely related to different bathymetry boundary conditions. For instance, due to the lack of a widely available Eocene bathymetry reconstruction, most earlier modelling studies used modern-day bathymetry with local modifications, which may be problematic because the impact of straits and other paleogeographic features on ocean

circulation are coupled (e.g. Ladant et al., 2018; Yang et al., 2014). Therefore, these various model configurations make it difficult to address questions on the potential states of the Eocene overturning circulation. Inter-model comparisons of results, using the same set of paleogeographic boundary protocols, can overcome this obstacle, improve the robustness of interpretations and narrow the range of uncertainties.

Within the Deep-Time Model Intercomparison Project (DeepMIP, https://www.deepmip.org/), a group of model simulations, including CESM1.2 (hereafter CESM), COSMOS, GFDL-CM2.1 (hereafter GFDL), IPSL-CM5A2 (hereafter IPSL), MIROC4m (hereafter MIROC), HadCM3B(L), NorESM1-F (hereafter NorESM) and INMCM, has been conducted with the early Eocene extreme warmth boundary conditions. The large-scale features of surface temperature in these simulations are presented in Lunt et al. (2021). The aim of this study is to explore Eocene ocean circulation, by comparing global ocean circulation in these DeepMIP simulations (except INMCM, which only carried out a simulation at 6x (1680 ppm) pre-industrial CO<sub>2</sub> concentration). Our goal is to determine the most likely overturning circulation state from the various independent model results, and further integrate them with knowledge from proxy data. For consistency in climate forcing, we focus mainly on the 3x CO<sub>2</sub> experiments for the intercomparison, which are available for nearly all of the DeepMIP models.

Following this introduction (Section 1) the paper is divided into three additional sections. Section 2 provides a brief summary of the models used and describes the simulation setup. Section 3 presents the model results of the globally integrated MOC. This includes identifying the MOC features shared across models, discussing inter-model comparison and analyzing MOC responses to different atmospheric CO<sub>2</sub> concentrations. This section ends with a narrative that provides an integrated perspective on proxy and model evidence for early Eocene ocean circulation. The conclusions are presented in Section 4.

#### 2 Models and simulations

The nine climate models in the DeepMIP and the Eocene simulations are documented in detail in Lunt et al. (2021). Here, we briefly summarize the models and simulation setups with a focus on the ocean components.

## 2.1 DeepMIP models

The DeepMIP models are all coupled Earth system models, including CESM1.2, COSMOS, GFDL-CM2.1, HadCM3B, HadCM3BL, IPSL-CM5A2, MIROC4m, NorESM1-F and INMCM. The main components of the Earth system are represented by relevant modules, as listed in Table S1. Key information on the ocean components and the associated sea ice modules is also summarized in Table S1. The ocean spatial resolution and the parameterization of diapycnal mixing varies widely across models, as summarized in Table S1 and described in SI.

#### 2.2 Simulation setup

The DeepMIP simulations are designed to simulate the early Eocene period of extreme warmth. The main changes in boundary conditions from the pre-industrial (PI) period include the specification of Eocene bathymetry, paleogeography and varied atmospheric CO<sub>2</sub> concentrations. Following Lunt et al. (2017), simulations employed bathymetry protocols in a hotspot reference frame (Herold et al., 2014), except for the NorESM simulation, which used a paleomagnetic reference bathymetry frame (van Hinsbergen et al., 2015). These two frames differ slightly, such as in the angle of rotation of the Antarctic continent and widths of the Drake Passage and Tasman Gateway (Fig. S1). The general bathymetries on individual model grids are comparable except for some detailed differences around straits due to multiple reasons (e.g. different bathymetry frames and various model resolutions as explained in Section 3.2.2). The bathymetry in the Southern Ocean of each model is provided in the SI (Fig. S1) with their strait geometry

summarized in Figure 4A and 4B. Regarding the atmospheric CO<sub>2</sub> concentration, the main Eocene control simulation was run at 840 ppm (three times the PI level, labelled as 3x). In addition to the main simulation, a set of CO<sub>2</sub> sensitivity experiments are included for each model (Table S1). All models have simulations with CO<sub>2</sub> concentrations ranging from 280 ppm (i.e. PI levels) to 840 ppm (or even higher). The GFDL and CESM simulations extended CO<sub>2</sub> concentrations to 6x and 9x, respectively. The NorESM simulations were run with 2x and 4x CO<sub>2</sub> levels (as the main Eocene simulation). INMCM was excluded from the analysis, because only a 6x CO<sub>2</sub> simulation was run, in which large uncertainties start to emerge. A PI simulation was run for all models, with PI bathymetry and 1x CO<sub>2</sub>.

The initial ocean temperature and salinity in simulations were set approximately following Lunt et al. (2017). Briefly, the initial temperatures were latitude- and depth-dependent with a globally averaged value ranging from 5°C (MIROC) to 17°C (CESM) (Table S1 and Fig. S2). The initial salinity was homogeneously set to a value of 34.7 psu in most of the simulations, except for CESM, which uses a larger value of 35.4 psu, and NorESM, which uses a smaller value of ~34.2 psu (Table. S1). The Eocene boundary conditions, which are significantly different from those of the present day, imply that simulations will require a long time to reach an equilibrium state (Kennedy-Asser et al., 2020). The simulation lengths varied from 2000 years in CESM and NorESM to over 7000 years in COSMOS (Table S1). Examination of the changes in temperature shows that most simulations reached quasi-equilibrium states with remaining deep-ocean temperature drifts over the last 1000 years being less than 0.5°C, except for the CESM and NorESM simulations with higher CO<sub>2</sub> levels (e.g. 1.1°C in CESM-3x and 0.7°C in NorESM-4x Fig. S2).

#### 3 Results and discussion

### 3.1 The overall pattern and strength of the global MOC

# 3.1.1 Modern overturning circulation

Before exploring the Eocene ocean circulation in the models, it is important to first evaluate the models' performance under known modern conditions. The simulated global MOC is presented by the classical streamfunction in the (westward-facing) latitude-depth plane (Fig. 1A), which was computed using the full meridional velocity fields (including separate Eulerian velocity and Bolus velocity in nearly all models). The PI global MOC in all models is composed of the traditional upper and lower cells associated with bipolar deep convection (Fig. 1). The location of deep convection is indicated by the deepest mixed layer depth (MLD) in the simulations, although the absolute MLD values are not exactly comparable across the models (e.g. an overall smaller MLD values in HadCM3B than in the other models) due to different cut-off values being employed to define the MLD in different models.

The upper MOC cell, as shown by positive streamfunction values, circulates clockwise (positive values) and is supplied by North Atlantic Deep Water (NADW) primarily formed in the Nordic Seas (Fig. 1B). The NADW propagates southward and forms a lower branch of the Atlantic Meridional Overturning Circulation (AMOC). There is good inter-model agreement in the general AMOC structure with the maximum flow being reached north of 40°N around 1 km depth (separated AMOC not shown here), which also fits the observed AMOC structure (e.g. Lumpkin and Speer, 2007). The simulated AMOC strength varies from 10 Sv in HadCM3BL to 24 Sv in CESM and GFDL, while the remaining models producing an AMOC intensity of 12-16 Sv. The latter group is close to the range of observations, 17±3 Sv (Lumpkin and Speer, 2007),

which might imply that we can perhaps have higher confidence in their simulations on AMOC intensity.

The lower cell circulates anticlockwise (negative values) and is fed by the bottom waters formed around Antarctica (AABW). The maximum streamfunction value of this lower cell is reached below 3 km depth at varied latitudes ranging from 65°S to 35°S. This range probably corresponds to two cores of overturning streamfunction in density and pressure levels (Lumpkin and Speer, 2007). Three models (IPSL, COSMOS and GFDL) simulate those two-core structures, while other models simulate a dominant bottom core. This seems to imply a better performance of the first group, but the wind-driven Deacon cell issue may complicate the comparison (Döös & Webb, 1994). AABW strength varies between models (Fig. 1). This lower cell strength is relatively weak (6-8 Sv; Table S2) in CESM, COSMOS and GFDL, but the remaining two models (IPSL and MIROC) show a stronger rate of deepwater formation (16-17 Sv; Table S2). With a large uncertainty range, the observation-based estimates (21±7 Sv, as summarized in Table S2) suggest a strength similar to the model of the latter group (Orsi et al., 1999). When considering both structure and strength, IPSL probably is reasonable for simulating the lower MOC cell, although the larger uncertainty ranges in the observation themselves need to be taken into account.

#### 3.1.2 Eocene overturning circulation

233

234

235

236

237

238

239

240

241

242

243

244

245

246

247

248

249

250

251

252

253

254

255

In the Eocene simulations, the overall structure of the MOC in most models (i.e., six out of eight, with two exceptions being GFDL and NorESM) is dominated by a single inter-hemispheric overturning cell with deep water generally forming in the Southern Ocean. This Southern Ocean cell is henceforth referred to as SO-MOC. (Fig. 2). In these six models, MLD values indicate deep water formation in the Pacific sector in the COSMOS simulation, in the Atlantic and Indian sectors in the CESM and

HadCM3B(L) simulations, and in all three SO sectors (Atlantic, Indian, Pacific) for the IPSL and MIROC simulations (Fig. 2B). Deepwaters then spread northward below ~2000 m, and fill individual oceans. The SO-MOC is associated with an upwelling branch extending over the whole Northern Hemisphere, closing the anti-clockwise overturning circulation. The strength of this SO-MOC in these models varies, ranging from 33 Sv in IPSL to 28 Sv in CESM and COSMOS to 12 Sv in HadCM3B(L). The maximum SO-MOC value is reached at latitudes of 61-67°S and at depths of 1.2-2.4 km.

In contrast to these six models, the two other models (GFDL and NorESM) show different global MOC results. The global MOC of the GFDL is dominated by a clockwise circulation, similar to today, but with a deep MLD in the Pacific (Fig. 2B) and a Pacific meridional overturning circulation (PMOC in Fig. 3). A maximum PMOC of 16 Sv is reached at 57°N at a depth of 0.7 km (Fig. 3). Compared to the vigorous deep convection exhibited in the other models, the abyssal ocean in the NorESM runs is almost stagnant with a weak abyssal circulation (4 Sv) at ~60°S. The main feature of the NorESM simulation is the shallow-to-intermediate waters (e.g., upper 1 km), formed in the North Atlantic with a maximum of 18 Sv (Fig. 3).

None of the models show deep overturning circulation (below 2000 m) in the open North Atlantic (Fig. 3). This is likely due to a combination of freshwater forcing and the basin geometry being unfavorable. The early Eocene North Atlantic has a much reduced width compared with modern day, and is restricted to mid-to-low latitudes (Herold et al., 2014). Moreover, north of approximately 40°N, the Atlantic receives a large freshwater flux input (Table 1), from both sides of the basins (Fig.S4a). In addition, there is a substantial outflow of fresh surface waters from the Arctic, due to the geometry of the Eocene Arctic Ocean (Hutchinson et al., 2018). This outflow of freshwater greatly reduces North Atlantic salinity and thus low surface water density, probably prevents deep water from forming in the Atlantic (Coxall et al., 2018, Hutchinson et al., 2019; Roberts et al., 2009; Stärz et al., 2017; Vahlenkamp et al., 2018).

MIROC and NorESM simulations show an intermediate overturning circulation (Fig. 3) with dense water forming in the Labrador Sea, specifically on the continental shelf of Baffin Bay (Fig. 2B). The continental shelf may provide a favorable basin condition for deepwater formation through so-called cascading or slip-down process (Marson et al., 2017), which is a different process to generate deep convection compared with open ocean convection. Cold and salty water formed in winter, associated with cooling, can mix with ambient water, producing a plume that overflows and slides down the slope as a gravity current. As shown in MIROC and NorESM, the high latitude (up to 75°N) of Baffin Bay can be a suitable region for deepwater formation as long as the surface forcing allows it, as will be discussed in Section 3.2.1. Deepwater formation and export in the Labrador Sea during the early and middle Eocene, however, is not supported by sedimentary or geochemical data, which imply relatively restricted and stagnant conditions in the basin (Cramwinckel et al., 2020; Kaminski et al., 1989).

One hypothesis emerged earlier to explain warm bottom waters during the early Cenozoic suggesting warm saline deep water (WSDW) in low latitudes, such as in the Tethys Ocean (Brass et al., 1982; Barron and Peterson 1991; Wright and Miller 1993; Huber & Sloan 2001). However, with the early Eocene bathymetry, DeepMIP models simulate no WSDW sinking in the Tethys or elsewhere in tropical regions, probably due to an unfavorable continental configuration (i.e. restricted Tethys Ocean).

#### 3.2 Explaining the inter-model spread

The large spread of model results for global MOC strengths can be due to a range of factors that involve the interplay of dynamic and thermodynamic processes in the ocean and atmosphere. Below, we explain this inter-model spread by examining the main factors of the air-sea interaction, strait geometry and divergent diapycnal mixing.

#### 3.2.1 Sea-surface freshwater flux

301

302

303

304

305

306

307

308

309

310

311

312

313

314

315

316

317

318

319

320

321

322

323

Previous studies have demonstrated the key role of local sea-surface freshwater forcing in determining the location of deepwater formation. The asymmetric deepwater formation between the North Pacific and North Atlantic under present-day conditions has been partly attributed to the differences in sea-surface freshwater forcing and the resulting ocean salinity (Craig et al., 2017; Ferreira et al., 2018; Zaucker et al., 1994). Intriguingly, a recent modelling study found that the redistribution of rainfall induced by the Rocky Mountains between the two basins may be a key to this asymmetry and that the artificial removal of the mountain range transfers the deep convection from the North Atlantic to the North Pacific (Maffre et al., 2018). The Rocky Mountains have existed from ca. 80-85 Ma (English & Johnston, 2004). They may have thus been routing freshwater into the Pacific since this time, although the effect was likely reduced in the early Eocene compared to the mid and late Eocene, when further uplift of the Central Rocky Mountains and adjacent Great Plains occurred (Fan & Carrapa, 2014). A more direct link between the freshwater flux and deepwater formation has been reported by Baatsen et al. (2018). They found that a relocation of 1 Sv freshwater flux from the South Pacific to the North Pacific can shift the deepwater formation from the North Pacific to the South Pacific under late Eocene climate conditions (38 Ma).

Freshwater exchange with the atmosphere and continental river runoff is the only external forcings on the surface salinity in the early Eocene, when the climate was too warm to allow sea ice in deepwater formation regions. Changes in sea-surface freshwater flux on the basin scale can trigger deep convection and deepwater formation via strong modification of surface ocean salinity (Zhang et al., 2020). The net air-sea freshwater flux is expressed as precipitation plus runoff minus evaporation, representing the net freshwater flux into the ocean with positive values

indicating water gain in this study. The freshwater flux map (Fig. S3A) shows that large scale patterns are dominant by various components and consistent with general modern climate patterns (e.g. equatorial rainfall and subtropical dry zone).

324

325

326

327

328

329

330

331

332

333

334

335

336

337

338

339

340

341

342

343

344

345

346

To quantitatively link freshwater flux to deepwater formation, we calculated the FWF budget of several regions that potentially host deepwater formation (Table 1). These regions include the North Pacific, North Atlantic, South Pacific, South Atlantic and South Indian Ocean, as indicated in Figure 2B. The absolute freshwater flux budget differs between the individual simulations, which complicates the inter-model comparison. However, the relative differences between regions of each model are good indicators of deepwater formation. The smallest freshwater flux value, representing the least freshwater gain in the ocean, points to the basin hosting deepwater formation, in particular for basins with clear, closed boundaries. For GFDL, the smallest freshwater flux value is found in the North Pacific (0.51 m/yr); for both CESM and IPSL, it is found in the South Atlantic (0.59 and 0.46 m/yr); and for COSMOS, it is found in the South Pacific (0.83 m/yr). All areas with minimal freshwater flux gain exhibit deepwater formation (Fig. 2B & Table 1). The coexisting relationship between the smallest freshwater gain budget and deep convection further highlights the key role played by freshwater flux in deepwater formation. We note however that the overall freshwater flux budget can be both a forcing factor and a diagnostic indicator of ocean advection feedback, due to the presence or absence of overturning circulation (Ferreira et al., 2018).

#### 3.2.2 Strait geometry constraints on deepwater formation

The role of strait geometry in regulating inter-basin exchange of water masses of different salinities (Fig. S4B) and ultimately in constraining the location of deepwater formation is clearly reflected in the results. Despite the common bathymetry protocol of Herold et al.

(2014), the actual configurations of the straits in individual simulations differ slightly due to differences in model resolution and choices made when converting the paleogeography to a model grid (Fig. 4). All of the ocean models used in DeepMIP require some manual adjustment when generating a practical paleogeography. For instance, the models require a minimum strait width of two grid cells so as to have non-zero velocity through the strait, and some degree of arbitrary choice is required to satisfy this condition, which leads to slightly different final strait configurations in each model. In general, coarser resolution models tend to have wider straits due to the requirement of at least two grid cells (Fig. 4A & 4B).

347

348

349

350

351

352

353

354

355

356

357

358

359

360

361

362

363

364

365

366

367

368

369

The net transports through the main straits, including the Drake Passage, the Tasman Gateway, the Panama Seaway and the Strait of Gibraltar, in the DeepMIP simulations are summarized in Table S3, and are crucial for controlling the degree to which seawater in adjacent basins differ in salinity. According to their geographical locations, these straits can be divided into two groups: high-latitude straits and tropical straits. For the high latitude straits (i.e., Drake Passage and Tasman Gateway), inter-basin exchange plays an important role in setting the location of deepwater formation in the Southern Ocean. Inter-basin exchange of seawater with different salinities (Fig. S4B) may modify the salinity budget in a basin, which is a key for setting up vertical stratification (e.g. Wolfe & Cessi, 2014). Inter-basin exchange in the Southern Ocean is accommodated by a shallow eastward-flowing proto-Antarctic Circumpolar Current (at bit shallow depth). The strength of the oceanic current approximately follows the size of the strait in the models (defined as width\*depth). For the Tasman Gateway, the current strength ranges from 1 Sv in CESM, IPSL, GFDL to 17 Sv in HadCM3BL (Fig. 4C). The Tasman Gateway in COSMOS is closed and thus freshwater (as shown in Fig. 4B & S4B) is prohibited from entering the South Pacific basin, which favors strong deep convection there. By contrast,

the open Tasman Gateway in other simulations allows for eastward currents that weaken or prohibit Pacific deepwater formation in the South Pacific. A wider Tasman Gateway in HadCM3B and HadCM3BL (compared with the other models) allows for stronger eastward flow of relatively fresh water that hinders active deep convection in the South Pacific sector. For the Drake Passage, all models suggest eastward transport with the highest strengths of up to 14 and 26 Sv in HadCM3B and HadCM3BL, respectively. This strong eastward transport in HadCM3B and HadCM3BL is associated with their deeper Drake Passage, despite a width similar to those of other models (Fig. 4A). Dinocyst assemblages from the early-middle Eocene suggest that the Tasman Gateway was closed prior to ~50 Ma (Bijl et al, 2013). Inter-basin thermal differentiation and geochemical proxy data suggest that Drake Passage has remained closed until the middle to late Eocene, as reviewed by Toumoulin et al., (2021). This observation, combined with the DeepMIP model results, suggests that favorable conditions for South Pacific deepwater formation existed in the early Eocene.

Compared with these high-latitude straits, the effects of tropical straits in explaining inter-model variation of deepwater formation are more indirect and less clear, due to the complexity of teleconnections between the tropics and deepwater formation regions. The models show a large variation in net volume transports across the Panama Seaway, ranging from 13 Sv eastward transport in COSMOS to 24 Sv westward transport in GFDL. Like the high-latitude straits, these differences are probably associated with differences in model configurations, as well as the alignment of straits with easterly trade winds. In addition, a previous relationship analysis (Omta & Dijkstra, 2003) showed that the transport through the Panama Seaway is also linearly related to the transport through both the Tethys Seaway and the Drake Passage. For instance, strong westward transport in NorESM and GFDL is seemingly related to strong

currents across the Gibraltar, although the different model-grid configurations make this intermodel comparison difficult (Table S3). For the Strait of Gibraltar, all simulations show westward transport, with the strength ranging from 9 Sv in CESM and COSMOS to 24 Sv in NorESM. Comparing these different transports with the MOC results, we do not find any clear indication that transport through straits relates to overturning strength directly.

393

394

395

396

397

398

399

400

401

402

403

404

405

406

407

408

409

410

411

412

413

414

415

Open tropical straits allow for considerable zonal water mass transport during the Eocene, which coexists with convection in one hemisphere. This observation contrasts with the bipolar mode of convection during the PI period, when tropical east-west transport was absent. We therefore suggest that the vigorous transport through tropical straits during the Eocene may have favored unipolar convection, although variations in the intensity of the hydrological cycle may affect this transport under different CO<sub>2</sub> levels (see Section 3.3). Vigorous east-west currents are likely to prevent the water masses above the strait depth from crossing the equatorial region and so that convection is favored in just one polar region. The unipolar convection model implies a different closure scheme from the present-day context, for example sinking water was supplied by water mass flow from other places where deepwater come out into shallow depth, rather than from inter-hemisphere flow (Zhang et al., 2021). This hypothesis also seems compatible with previous studies on the effects of open and closed straits. For instance, Yang et al. (2014) found that an open Panama Seaway, together with a closed Drake Passage, can promote the emergence of single-cell circulation (in the latitude-depth plane) with deepwater formation in the Southern Ocean by suppressing NADW formation. Moreover, Zhang et al. (2012) proposed that the closing of tropical seaways invokes the transition of ocean circulation from a Southern Ocean deepwater-dominated mode to a modern-like ocean circulation with bipolar convection (i.e. both NADW and AABW formation). Nevertheless, there are also models, such as the late Eocene (38 Ma) GFDL model, which found bipolar convection in Pacific basin with an open Panama Seaway (Hutchinson et al., 2019).

## 3.2.3 The role of salt-advection in maintaining deepwater formation

416

417

418

419

420

421

422

423

424

425

426

427

428

429

430

431

432

433

434

435

436

437

438

Once the ocean circulation differences are set by "external" factors, such as the atmospheric freshwater forcing and geometry differences discussed above, they can be maintained by heat and salt-advection feedbacks, similar to the present-day Atlantic MOC (Ferreira et al., 2018). As a result of horizontal exchange with the ambient ocean and the vertical interaction with the atmosphere, salinity is often used as an important tracer to diagnose ocean circulation patterns. Salinity also impacts density and thus stratification of the water column in cold high-latitude regions where deep water can be formed. In this sense, relatively high seasurface salinity (SSS) discloses places where salt-advection feedbacks occur. For the PI simulation, all the DeepMIP models reproduce substantially enhanced SSS in the North Atlantic (highlighted by thick lines in Fig. 5A) compared with the North Pacific, with "double saddles" latitudinal-wise peaking (up to 36 psu) at the latitudes of ~30°N/S, although absolute salinity values vary between models. For the North Atlantic basin, all models' salinities are within 1 psu of observations at the PI. By contrast, some obvious inter-model differences are found in the Pacific basin. In particular, HadCM3BL shows a fresher North Pacific than other models and the observations by over 2 psu (up to 5 psu at 60°N). This overall low Pacific salinity in HadCM3BL has been noted in an earlier study (Valdes et al., 2017) and is mainly due to freshwater input from the surrounding continents. The freshwater input seems also related to its coarse resolution, since such salinity bias is much smaller in the higher resolution version HadCM3B. To summarize, most of the models are within 1 psu of observations at the PI and not obviously better than others, except for the HadCM3BL model which has some biases in its hydrological cycle at high latitudes, implying its Eocene MOC values in the Pacific may have greater uncertainty than in the other models.

439

440

441

442

443

444

445

446

447

448

449

450

451

452

453

454

455

456

457

458

459

460

461

Similar to the present day, the early Eocene SSS spatial patterns, to first order, are a "double-saddle" latitudinal variation that is primarily controlled by freshwater flux from the atmosphere. More importantly, the basin scale SSS differences are noticeable, which is indicative of whether deepwater formation is confined to a particular basin among individual models and also distinguishes the locations of deepwater formation within a model. In most cases, relatively high salinity values in the high latitudes (highlighted by thick lines in Figure 5B) reflect the presence of deepwater formation. In the North Pacific basin, the GFDL simulation shows the highest salinity and exceptional deepwater formation compared with other models. In the South Pacific, COSMOS, IPSL and MIROC show higher salinity than other models, which is consistent with deep convection occurring there. Similarly, the high salinity of the North Atlantic in NorESM and MIROC, and of the South Atlantic in CESM and IPSL indicate convection in these regions. It is worth mentioning that such a relationship between the salinity and deepwater formation is exceptionally unclear in HadCM3B, probably because of its salinity bias as discussed above. In other words, a fresh salinity bias in the North Pacific would prevent deep convection there.

## 3.2.4 Divergent diapycnal mixing parameterization

Diapycnal mixing can strongly affect the overturning circulation by reducing density and raising the buoyancy of the abyssal water near the rough bottom, providing the necessary upward motion of deep water needed to counterbalance the downward flow of cold and dense deep water at high latitudes (Munk, 1966; Munk & Wunsch, 1998) and in the interior by mixing (Ferrari et al., 2016; de Lavergne et al., 2017). Previous studies have quantitatively linked tracer diffusion,

as a parameterized process contributing to diapycnal mixing in the model, to the strength of the overturning circulation. With some simplifications, the strength of the overturning circulation is proportional to the diffusivity coefficient ( $Kv^{2/3}$ ), both in theoretical and idealized model simulations (Nikurashin & Vallis, 2011). For example, Thomas et al. (2014) used the MITGCM model to test the effect of different degrees of diffusion on ocean circulation during the early Cenozoic and found a circulation response very sensitive to vertical diffusivity.

462

463

464

465

466

467

468

469

470

471

472

473

474

475

476

477

478

479

480

481

482

483

484

With various parameterization schemes among the models (summarized in SI), vertical diffusion decreases along the depth of the water column with intense diffusivity at the surface mixed layer and weak diffusion below the thermocline (Fig. S4). The horizontally averaged vertical diffusion can vary by as much as two orders of magnitude across these models (Fig. S4B). The magnitudes of these upper enhancements vary among the models due to different parameterization schemes used in simulations (Table S1). The diffusion in the Richardson number-dependent parameterization scheme (known as PP scheme, see Pacanowski & Philander, 1981 for more details), as used in the HadCM3 and MIROC models, is generally weaker than in models with explicitly incorporated diffusion, such as CESM, COSMOS and IPSL. In particular, at depths of 500 m to 3500 m, diffusivity ranges from 10<sup>-4</sup> m s<sup>-2</sup> in HadCM3 and MIROC to 10<sup>-2</sup> m s<sup>-2</sup> in CESM, COSMOS and IPSL. The geographical pattern of this tracer diffusion is depthdependent. The strong diffusion in the upper ocean is most obvious over regions of deep convection. At greater depths (e.g. 4000 m, as in Fig. S4B), diffusion is enhanced near rough bottom topography features, which is consistent with our understanding of strong vertical mixing in the deep oceans (Ferrari et al., 2016; Ledwell et al., 2000).

Enhanced diapycnal mixing seems to lead to increased global MOC strength within simulations performed with models using the same parameterization schemes. For example, the

slightly stronger MOC in HadCM3B compared with that in HadCM3BL (due to removal of the Richardson number dependency; see Valdes et al., 2017) is in line with the enhanced vertical diffusion of HadCM3B (Fig. S4). Furthermore, the additional tidal mixing that was not taken into consideration in simulations contributes to 7 Sv of the Southern Ocean MOC in the IPSL simulation by enhanced abyssal diffusivity (Fig. S5). However, it is not straightforward to apply this relationship across all models, which use different mixing schemes. Models are tuned to reproduce realistic ocean circulation under PI conditions, and with many different model-grid configurations and parameterization schemes, which are not directly comparable with one another.

## 3.3 Global MOC response to atmospheric CO<sub>2</sub> level for the early Eocene

Results show that the structure and strength of the global MOC for most DeepMIP simulations (all except CESM and GFDL) are relatively stable over a range of atmospheric CO<sub>2</sub> concentrations, from 1x to 4x PI levels (Fig. 6). Overall, the simulated SO-MOC exhibits a similar structure across multiple CO<sub>2</sub> levels up to 3x (at least) with minor changes in circulation strength. GFDL simulations are the exception, because they feature a very weak South Pacific sinking at 1x and 2x CO<sub>2</sub>, but not from 3x CO<sub>2</sub> upward, whereas the PMOC remains active throughout. The change in South Pacific sinking in the GFDL model is in line with their much-reduced surface freshwater flux (0.35 m/yr and 0.57 m/yr in 1x and 3x, respectively). This is likely related to the presence of sea ice at lower CO<sub>2</sub> levels, which then disappears at higher levels of CO<sub>2</sub> (not shown), as discussed by Hutchinson et al. (2018). Another exception is intermediate water formation in CESM, which shifts from the North Atlantic to the North Pacific when CO<sub>2</sub> is increased from 1x to 3x (see also Fig. 2B). This reorganization of intermediate water formation in CESM is likely associated with changes in the inter-basin atmospheric

moisture transport under different CO<sub>2</sub> levels, which is consistent with the surface evaporation flux (as defined by the residual of total freshwater flux minus precipitation; Fig. S6). A similar switch from North Atlantic to North Pacific convection has been reported in a previous modelling study using CESM with an increase of CO<sub>2</sub> from 280 ppm to 400 ppm and a PI bathymetry configuration (Burls et al., 2017). These similarities suggest that inter-basin variation in Northern Hemisphere intermediate water formation may be a unique feature of the CESM model.

In extremely high CO<sub>2</sub> (6x) simulations, the abyssal MOC in CESM collapses due to a highly stratified ocean. This is likely due to the relatively short simulation length of CESM and its initiation from cooler than equilibrium conditions, as indicated by the fact that the deep ocean is warming at the end of the simulation (Zhu et al., 2019) (see also Fig. S2A). This cooler deep water and relative warmer surface produce a stable water column that could restrict vertical convection. In contrast, in the GFDL 6x CO<sub>2</sub> simulation, the North Pacific MOC has a similar strength to that under lower levels of CO<sub>2</sub>. This difference is mainly due to the fact that the GFDL 6x CO<sub>2</sub> simulation was initiated from warmer-than-equilibrium conditions, meaning the deep ocean is able to lose heat through the overturning circulation when approaching equilibrium and the convection process can take place.

One interesting observation is that the models simulate convection in just one hemisphere for the Eocene-1x simulations (i.e. the same CO<sub>2</sub> as the PI period), which is in the Southern Ocean with northward propagation of dense water in the abyss of major ocean basins. Except for CESM and NorESM, there is no convection in the North Atlantic. The absence of North Atlantic convection in the high-CO<sub>2</sub> Eocene simulations (compared with the modern Atlantic MOC) is therefore unrelated to higher CO<sub>2</sub> levels, but rather due to other different factors, such as ice

sheets, paleogeography and bathymetry. Given that the Eocene global MOC is forced differently from the PI global MOC, its sensitivity to CO<sub>2</sub> forcing is not directly applicable to present-day and future circulation. However, for discussion of future climate change, it may still be informative to compare the structure of the global MOC in low and high CO<sub>2</sub> forcing scenarios, for example, in response to freshwater forcing.

Unipolar Southern Ocean sinking would imply no northward oceanic heat transport from meridional ocean overturning, so that Eocene Arctic polar amplification would have to be explained by other processes such as alternative wind-driven ocean heat transport, atmospheric heat transport, or local radiative heat balance over the Arctic.

Comparing with earlier studies, our analysis of the DeepMIP simulations (using comparable setups and boundary conditions) takes a step forward and reveals a non-linear global MOC response to CO<sub>2</sub> forcing, with a muted response in global MOC at elevated levels of CO<sub>2</sub>, from 1x (or 1.5x in IPSL) to 3x (or 4x in NorESM) in most models, and divergent responses at high CO<sub>2</sub> levels of 6x (compare CESM with GFDL). From a geological perspective, these intermodel simulations under different CO<sub>2</sub> levels can be seen as analogues for multiple time intervals of the Eocene prior to major paleogeographic changes (e.g. the Oligocene opening of the Tasman Gateway). In this sense, the muted global MOC response over a lower range of CO<sub>2</sub> may suggest that the SO-MOC dominated the global basin with northward currents prevailing in the abyss at multiple time intervals during the Eocene. In general, the observed insensitivity of the global MOC to CO<sub>2</sub> changes may imply that ocean circulation was relatively stable before the Oligocene, although the global MOC response to carbon cycle perturbations such as those during the Paleocene-Eocene Thermal Maximum (PETM), which experienced very high CO<sub>2</sub> levels, remains inconclusive.

## 3.4 Proxy-based records of ocean circulation

In order to evaluate the model results, we consider the proxy data constraints available for early Eocene deepwater circulation. The Eocene deep-sea sedimentary archives are generally sparse, with relatively poor spatial and/or temporal coverage and large uncertainties in chronologies. Especially lacking are high-quality sequences from high-latitude regions of potential deepwater formation. Nonetheless, a broad picture of ocean structure, alluding to the mode of the overturning circulation in individual ocean basins, can be reconstructed. We here use data from two independent deepwater proxies: (i) stable carbon isotope ratios ( $\delta^{13}$ C) from benthic foraminifera calcite and (ii) fish debris neodymium (Nd) isotope signatures, where Nd isotopes are expressed in the epsilon notation,  $\varepsilon_{Nd}$ , as the deviation of a measured  $^{143}$ Nd/ $^{144}$ Nd ratio from the "bulk earth" value in parts per 10,000.

# Carbon isotopes

In the modern ocean, high  $\delta^{13}C$  of ocean dissolved inorganic carbon (DIC), correlates closely with low nutrients such as phosphate [PO<sub>4</sub>], and vice versa (Kroopnick, 1985; Lynch-Stieglitz et al., 2007). This arises from surface primary producers taking up nutrients and carbon, preferentially removing the light carbon isotope ( $^{12}C$ ). Subsequent remineralization of organic matter in deeper waters releases nutrients and  $^{12}C$ -enriched carbon, imparting a relatively low DIC  $\delta^{13}C$  signature at depth, that is imprinted into the CaCO<sub>3</sub> isotopic chemistry of benthic foraminifera shells. Because modern NADW and AABW are formed from source waters with contrasting preformed nutrient states (low versus high, respectively), they have contrasting  $\delta^{13}C$  signatures. Therefore, at any single location in the Atlantic, deep water is strongly influenced by the relative mixing ratio of NADW (high  $\delta^{13}C$ ) and AABW (low  $\delta^{13}C$ ) (Kroopnick, 1985; Lynch-Stieglitz et al., 2007). Furthermore, within a given water mass, and along the main deep ocean

flow-path, progressive organic carbon remineralization gives rise to water mass ageing, which is detectable via a progressive decrease in DIC  $\delta^{13}$ C (Curry & Oppo, 2005; Lynch-Stieglitz et al., 2007). The large geographic separation of present-day ocean basins, and thus the long transit times for global deep waters (ca. 1000 years), enhances this process and creates distinct endmember North Atlantic and North Pacific  $\delta^{13}$ C signatures (Kroopnick, 1985).

577

578

579

580

581

582

583

584

585

586

587

588

589

590

591

592

593

594

595

596

597

598

599

In contrast to the present day, and even the late Eocene (Coxall et al., 2018; Cramer et al., 2009), existing early-Eocene benthic  $\delta^{13}$ C data from different basins are remarkably similar (Fig. 7A), suggesting a homogenous global deep ocean with respect to DIC  $\delta^{13}$ C (Cramer et al., 2009; Sexton et al., 2006). Hypothetically, and assuming minimal diagenetic issues, this observation can be explained by four possible circulation regimes. The first explanation (1) involves multiple, separate deepwater sources existing during the early Eocene, with limited opportunity for prolonged deepwater ageing to impart significant δ<sup>13</sup>C differences between them (Sexton et al., 2006). This would be consistent with an early Eocene paleogeography involving oceanic "short-cuts" between the major basins via tropical and boreal seaways that do not exist today. The second possibility is that multiple, distinct, vigorous and separate overturning circulations existing in each basin, but with limited inter-hemispheric transfer (requiring multiple sub-equator upwelling zones), similarly shortening the time scales for water mass  $\delta^{13}$ C ageing (Hutchinson et al., 2019; Lunt et al., 2010; Nisancioglu et al., 2003; Thomas et al., 2014). Regimes (1) and (2) would be expected to produce heterogeneity in deep-ocean  $\delta^{18}$ O due to contrasting temperature and salinity in the separate overturning cells and basin regions. However, the benthic  $\delta^{18}$ O data from different ocean basins yield a relatively homogenous signal (Sexton et al., 2006). Another possibility (3) is that The minimal early Eocene inter-basin benthic  $\delta^{13}$ C gradients could be caused by faster equilibration of atmospheric CO2 into the ocean mixed layer under high atmospheric pCO<sub>2</sub> of the early Eocene (Galbraith et al. 2015). This should serve to greatly decrease carbon isotopic disequilibrium, thereby theoretically weakening  $\delta^{13}$ C gradients within the ocean (Galbraith et al. 2015). Yet vertical (planktonic-benthic)  $\delta^{13}$ C gradients were much higher than modern in the early Eocene (Hilting et al., 2008; Sexton et al., 2006; Sexton et al., 2011), arguing against a faster ocean equilibration timescale of atmospheric CO<sub>2</sub> into the ocean as a potential explanation for the minimal lateral inter-basin  $\delta^{13}$ C gradients.

A fourth possibility (4) is that there was a single dominant deepwater source during the early Eocene, but with weak ageing gradients due to a less efficient "soft tissue" carbon pump than exists today (Sexton et al., 2006). This may have been a consequence of the different ocean circulation and nutrient distributions, as well as warmer ocean temperatures that elevated metabolic rates (Boscolo-Galazzo et al., 2018; Wilson et al., 2018).

Despite the overall minimal early Eocene benthic  $\delta^{13}$ C gradients, small inter-basin isotope differences of several tenths of a per mil are apparent (Fig. 7A) (Cramer et al., 2009; Sexton et al., 2006). These small inter-basin differences are often difficult to interpret unambiguously with regard to patterns of deepwater circulation. The  $\delta^{13}$ C data nevertheless point to an early-Eocene dominance of Southern Ocean sourced deep waters with a negligible contribution from the North Atlantic Ocean (D'haenens et al., 2014; Kaminski et al., 1989; Nunes & Norris, 2006; Pak & Miller, 1992). The earliest indications for the formation of North Atlantic-sourced deep waters from other (non- $\delta^{13}$ C) palaeoceanographic evidence is at the end of the early Eocene ~48 Ma (Boyle et al., 2017; Hohbein et al., 2012), roughly coincident with the onset of Cenozoic climatic cooling.

#### Neodymium isotopes

Another commonly used method for tracing deep water masses is Nd isotope analysis of fish teeth and debris. These materials acquire their Nd isotope signals post-mortem on the seafloor during early diagenesis (Martin & Haley, 2000; Martin & Scher, 2004). The captured signal is commonly interpreted as the bottom water Nd isotope ratio in the region of deposition, regardless of the behavioral patterns and habitats of the fish whilst alive. Neodymium is a lithogenic element, which is supplied to the ocean predominantly from the continents, which in turn carry characteristic isotopic fingerprints due to the age and lithology of the different local rock types (e.g. Robinson et al., 2021). Neodymium has a residence time in the ocean that is shorter than the global turnover time (~400 to 700 years; e.g. Tachikawa et al., 2003), allowing water masses to retain their unique isotopic ratio in the absence of additional Nd inputs. In the modern ocean, North Atlantic deep waters are characterized by  $\varepsilon_{Nd}$  values of -13, Southern Ocean deep waters are characterized by  $\varepsilon_{Nd}$  values of around -8, and Pacific waters show  $\varepsilon_{Nd}$ values of -4 (see the summary by van de Flierdt et al., 2016). These characteristic fingerprints mean that away from ocean margins, dissolved Nd isotopes can often indicate the provenance of water masses and, by inference, ocean circulation and water mass mixing (e.g., van de Flierdt et al., 2016; Frank, 2002; Goldstein & Hemming, 2014). This use of the  $\varepsilon_{Nd}$  proxy, however, hinges on the assumptions of constant endmembers through time and the absence of non-conservative processes affecting the signature in authigenic (i.e. seawater-derived) deposits (e.g. Haley et al., 2017).

622

623

624

625

626

627

628

629

630

631

632

633

634

635

636

637

638

639

640

641

642

643

644

A compilation of available authigenic Nd isotope data from  $\sim$ 30 global sites for an early-to-middle Eocene time frame of 54 to 45 Ma (Fig. S7) shows an  $\epsilon_{Nd}$  range from -1.1 (ODP Site 1001 on the Nicaraguan Rise) to -12.1 (ODP Sites 1258 and 1261 on the Demerara Rise) (n = 145). Focusing on results from open ocean sites in the Atlantic and Pacific Oceans, Figure 7B

reveals a clear dichotomy between Pacific and Atlantic Nd isotope signatures, similar to other times of the Mesozoic and Cenozoic (e.g. Frank, 2002; Voigt et al., 2013). The inter-basin distinction between the Atlantic and Pacific Oceans, a feature that is also observed in the modern oceans (e.g. van de Flierdt et al., 2016), indicates that Eocene sites from the Atlantic and Pacific Ocean were bathed in water influenced by inputs of differing  $\varepsilon_{Nd}$  characteristics. This could either serve as indication of multiple, independent sources of deepwater, or a single region of deepwater formation with basin specific Nd additions, for example benthic fluxes, imparting contrasting Nd isotope ratios in transition waters.

There is a general trend for  $\varepsilon_{Nd}$  values to become less radiogenic (i.e. lower) from the north to south in the Pacific basin (Fig. 7B; Hague et al., 2012; Thomas et al., 2014). Meanwhile, another way to describe the same data is to state that they become more radiogenic from the south to the north, given the fact that a gradient in a tracer can be created from both ends. There are three possible explanations for this observed trend: (1) export of less radiogenic Southern Ocean waters into the Pacific, (2) North Pacific deepwater formation with encroachment to the south or (3) a combination of the two, with deep convection in the North and South Pacific. All of these possibilities have been argued in the past (Huck et al., 2017; Hutchinson et al., 2018; Thomas, 2004; Thomas et al., 2014) and cannot be resolved with the data at hand (Fig. 7B).

Open ocean Atlantic Nd isotope data coverage for the early to middle Eocene is more limited, with only five locations, three at 1.5 to 2 km depth and two at 3.5 to 4 km depth (Fig. 7B; Scher & Martin, 2004; Thomas et al., 2003; Via & Thomas, 2006). At both distinct depths, there appears to be a general shift towards more radiogenic values from the south to the north, a trend that is more pronounced at the deeper sites (2 epsilon units), but less pronounced than what was observed in the Pacific Ocean. The weak gradient in authigenic Nd isotope values is

consistent with a Southern Ocean deepwater source. However, similar to the Pacific, it may also indicate convection of a radiogenic deepwater mass source in the North Atlantic. The latter seems unlikely, however, as present estimates place the onset of Northern Component Water in the middle to late Eocene (Boyle et al., 2017; Hohbein et al., 2012; Coxall et al., 2018; Gleason et al., 2009; Miller & Tucholke, 1983). Based on other studies, bottom water formation in the Atlantic sector of the Southern Ocean and northward export seems more feasible for the early to middle Eocene (e.g. Batenburg et al., 2018; Robinson et al., 2010; Thomas et al., 2003).

In summary, benthic foraminifera  $\delta^{13}C$  and fish teeth  $\epsilon_{Nd}$  provide a consistent picture of an absence of bipolar convection in the Atlantic Ocean in the early Eocene. Instead, strong Southern Hemisphere-driven overturning seems more likely. Data-based evidence for a North Pacific source is more ambiguous. Filling important data gaps in the northern North Atlantic, North Pacific and South Pacific across a suite of water depths and for a range of proxies will be crucial for depicting a more comprehensive picture of early Eocene ocean overturning.

# 3.5 Model-data comparison of Eocene ocean circulation

The models provide strong support for Southern Ocean convection and northward-flowing currents into the abyss of major ocean basins. A rather homogenous global ocean with respect to DIC  $\delta^{13}$ C suggests that there was a single dominant deepwater source, but with an ageing gradient weaker than that which exists today. Existing Nd isotope data are consistent with the idea of production and export of AABW into the Pacific and Atlantic Oceans. Therefore, a likely feature of the early Eocene is the sinking of dense water in the Southern Ocean and northward propagation, as seen from the various model outputs from the model inter-comparison and proxy reconstructions from benthic foraminifera  $\delta^{13}$ C and fish teeth  $\epsilon_{Nd}$ .

Compiled  $\varepsilon_{Nd}$  data would allow for early Eocene convection in the North Pacific, a result that is indicated by the GFDL model, but not in any of the other models. Thus, evidence for deepwater formation in the North Pacific basin is inconclusive. Models and geochemical proxydata ( $\varepsilon_{Nd}$  and benthic  $\delta^{13}$ C) agree that it is very unlikely that deep water formed in the North Atlantic during the early Eocene, unlike the modern day. Model results show no overturning in the open ocean of the North Atlantic probably due to a combination of freshwater forcing and basin geometry being unfavorable. Only two models show intermediate water formation on the continental shelf of Baffin Bay, which is, however, tied to strong freshwater exchange with the atmosphere.

#### 4. Conclusions

Six out of eight DeepMIP models, run under similar boundary conditions for the warm early Eocene, show an absence of deepwater sinking in the Northern Hemisphere and the presence of deepwater formation in the Southern Ocean (as summarized in Fig. 8). The sites of this Southern Ocean deepwater formation are located in different sectors in the individual models. HadCM3B(L) and CESM models show deepwater formation in the Indian and Atlantic sectors of the Southern Ocean, probably due to a rather fresh Pacific. The COSMOS model, on the other hand, indicates deepwater formation in the Pacific sector where relatively saline water is trapped by the closed Tasman Strait. The other two models (IPSL and MIROC) suggest deepwater formation in multiple sectors of the Southern Ocean. In summary, prior to the wide opening of Southern Ocean gateways, deep waters likely formed in different sectors, from where they were exported northward in the abyss and upwelled in the entire Northern Hemisphere. Further confirmation of this conclusion could be achieved using targeted proxy-data to constrain early Eocene upwelling distribution in future.

Proxy-based  $\delta^{13}$ C and  $\epsilon_{Nd}$  data are consistent with a southern origin of early Eocene deep water in the Atlantic basin and associated northward propagation at abyssal depths. By contrast, the direction of early Eocene flow of abyssal waters in the Pacific remains more uncertain. Although the  $^{13}$ C data indicate deepwater formed in the Southern high-latitude, Nd isotope data are inconclusive. Thus, South Atlantic deepwater formation and northward export appear to be robust features of the early Eocene, whereas more Nd data would be required to resolve the exact transport direction of abyssal water in the North Pacific.

Our further diagnosis of inter-model spreads of overturning circulation reveals that the different MOC modes among models are largely set by air-sea freshwater exchanges. This highlights the importance of a good representation of the hydrological cycle in models that aim to simulate ocean circulation. This is particularly crucial for geological periods of past warmth, as the hydrological cycle during such times was probably stronger than today, exaggerating biases in the cycle. Once freshwater fluxes and associated large-scale ocean circulation features are established, they can be maintained by the salt-advection feedback (e.g. Stommel feedback)

A detailed examination of the hydrological cycle across models would benefit of reducing model-dependent bias in the meridional ocean circulation, which should be the focus of future inter-model comparison analysis.

# Acknowledgments

- We acknowledge valuable contributions from anonymous reviewers and pertinent suggestions from the
- 733 Editor and associated Editor that have clarified and improved the manuscript. We would like to thank
- 734 Thierry Huck for discussions in the early stage of the analysis.
- YZ was supported by the Fundamental Research Funds for the Central University (grant no.
- 736 20720210079). AdB acknowledges funding from Swedish Research Council projects 2016-03912 and
- 737 2020-04791. DJL and SS acknowledge NERC grant NE/P01903X/1. DKH acknowledges funding from
- 738 FORMAS grant 2018-01621, and their GFDL model simulations were performed by resources provided

- by the Swedish National Infrastructure for Computing (SNIC) at the National Supercomputer Centre
- 740 (NSC), partially funded by the Swedish Research Council through grant agreement 2018-05973. PR and
- 741 TvdF acknowledge funding from NERC grant NE/ P019080/1. PS was supported by Natural Environment
- Research Council (NERC) Grant NE/P019331/1. HKC was supported by Swedish Research council (VR)
- 743 grant DNR 2014-4153. J-BL and YD acknowledge GENCI for providing access to the HPC resources of
- TGCC through allocation no. 2019-A0050102212, with which IPSL simulations were performed. JZ and
- CP acknowledge the support of the Heising-Simons Foundation (grant no. 2016-05 and 2016-12) and
- National Science Foundation (grant no. 2002397), as well as computational resources provided by the
- Computational and Information Systems Laboratory at the National Center for Atmospheric Research,
- which is a major facility sponsored by the NSF under Cooperative Agreement 1852977. WLC and Ayako
- Abe-Ouchi acknowledge funding from JSPS KAKENHI (grant no. 17H06104) and MEXT KAKENHI
- 750 (grant no. 17H06323), and are grateful to JAMSTEC for use of the Earth Simulator.

# Open Research

751

759

760

- The DeepMIP simulation data used in this study have been archived in the DeepMIP database. The
- database can be accessed by following the instructions at <a href="https://www.deepmip.org/data-eocene/">https://www.deepmip.org/data-eocene/</a>. In
- addition, temperature and radiative fluxes from the models can be downloaded directly from the
- Supplementary Information of Lunt et al. (2021). The compiled Nd proxy dataset is available from the
- supplementary information of this study, and all the original sources for the data are Hague et al. (2012),
- 757 Huck et al. (2017), MacLeod et al. (2011), Scher and Martin (2004), Thomas (2004), Thomas et al.
- 758 (2003), Thomas et al. (2008), Thomas et al. (2014) and Via and Thomas (2006).

## References

- Anagnostou, E., John, E. H., Babila, T. L., Sexton, P. F., Ridgwell, A., Lunt, D. J., et al. (2020). Proxy evidence for state-dependence of climate sensitivity in the Eocene greenhouse. *Nature Communications*, 11(1), 4436.
- 763 https://doi.org/10.1038/s41467-020-17887-x
- Baatsen, M., von der Heydt, A. S., Huber, M., Kliphuis, M. A., Bijl, P. K., Sluijs, A., & Dijkstra, H. A. (2020). The middle to late Eocene greenhouse climate modelled using the CESM 1.0.5. *Climate of the Past*, 16(6), 2573–2597. https://doi.org/10.5194/cp-16-2573-2020
- Baatsen, M. L. J., von der Heydt, A. S., Kliphuis, M., Viebahn, J., & Dijkstra, H. A. (2018). Multiple states in the late Eccene ocean circulation. *Global and Planetary Change*, *163*, 18–28.
- 769 https://doi.org/10.1016/j.gloplacha.2018.02.009
- Baatsen, M., van Hinsbergen, D. J. J., von der Heydt, A. S., Dijkstra, H. A., Sluijs, A., Abels, H. A., & Bijl, P. K. (2016).
   Reconstructing geographical boundary conditions for palaeoclimate modelling during the Cenozoic.
   Climate of the Past, 12(8), 1635–1644. https://doi.org/10.5194/cp-12-1635-2016
- Barnet, J. S. K., Littler, K., Westerhold, T., Kroon, D., Leng, M. J., Bailey, I., et al. (2019). A High-Fidelity Benthic
   Stable Isotope Record of Late Cretaceous Early Eocene Climate Change and CarbonSche Cycling.
   Paleoceanography and Paleoclimatology, 34(4), 672–691. https://doi.org/10.1029/2019PA003556
- 776 Barnet, James S.K., Littler, K., Kroon, D., Leng, M. J., Westerhold, T., Röhl, U., & Zachos, J. C. (2018). A new high-777 resolution chronology for the late Maastrichtian warming event: Establishing robust temporal links with 778 the onset of Deccan volcanism. *Geology*, 46(2), 147–150. https://doi.org/10.1130/G39771.1

- Batenburg, S. J., Voigt, S., Friedrich, O., Osborne, A. H., Bornemann, A., Klein, T., et al. (2018). Major intensification
   of Atlantic overturning circulation at the onset of Paleogene greenhouse warmth. *Nature Communications*, 9(1), 4954. https://doi.org/10.1038/s41467-018-07457-7
- 782 Bijl, P. K., Schouten, S., Sluijs, A., Reichart, G.-J., Zachos, J. C., & Brinkhuis, H. (2009). Early Palaeogene temperature 783 evolution of the southwest Pacific Ocean. *Nature*, 461(7265), 776–779. 784 https://doi.org/10.1038/nature08399
- 785 Bijl, P. K., Bendle, J. A. P., Bohaty, S. M., Pross, J., Schouten, S., Tauxe, L., et al. (2013). Eocene cooling linked to early flow across the Tasmanian Gateway. *Proceedings of the National Academy of Sciences*, 110(24), 9645–9650. https://doi.org/10.1073/pnas.1220872110
- Bornemann, A., D'haenens, S., Norris, R. D., & Speijer, R. P. (2016). The demise of the early Eocene greenhouse –
   Decoupled deep and surface water cooling in the eastern North Atlantic. *Global and Planetary Change*,
   145, 130–140. https://doi.org/10.1016/j.gloplacha.2016.08.010
- de Boer, A. M., Sigman, D. M., Toggweiler, J. R., & Russell, J. L. (2007). Effect of global ocean temperature change on deep ocean ventilation. *Paleoceanography*, 22(2), PA2210. https://doi.org/10.1029/2005PA001242
- Boscolo-Galazzo, F., Crichton, K. A., Barker, S., & Pearson, P. N. (2018). Temperature dependency of metabolic
   rates in the upper ocean: A positive feedback to global climate change? *Global and Planetary Change*,
   170, 201–212. https://doi.org/10.1016/j.gloplacha.2018.08.017
- Boyle, P. R., Romans, B. W., Tucholke, B. E., Norris, R. D., Swift, S. A., & Sexton, P. F. (2017). Cenozoic North Atlantic
   deep circulation history recorded in contourite drifts, offshore Newfoundland, Canada. *Marine Geology*,
   385, 185–203. https://doi.org/10.1016/j.margeo.2016.12.014
- Bryan, K., & Lewis, L. J. (1979). A water mass model of the World Ocean. *Journal of Geophysical Research*, 84(C5), 2503. https://doi.org/10.1029/JC084iC05p02503
- Chalk, T. B., Hain, M. P., Foster, G. L., Rohling, E. J., Sexton, P. F., Badger, M. P. S., et al. (2017). Causes of ice age intensification across the Mid-Pleistocene Transition. *Proceedings of the National Academy of Sciences*, 114(50), 13114–13119. https://doi.org/10.1073/pnas.1702143114
- Coxall, H. K., Huck, C. E., Huber, M., Lear, C. H., Legarda-Lisarri, A., O'Regan, M., et al. (2018). Export of nutrient rich
  Northern Component Water preceded early Oligocene Antarctic glaciation. *Nature Geoscience*, *11*(3),
  190–196. https://doi.org/10.1038/s41561-018-0069-9
- Craig, P. M., Ferreira, D., & Methven, J. (2017). The contrast between Atlantic and Pacific surface water fluxes.
   Tellus A: Dynamic Meteorology and Oceanography, 69(1), 1330454.
   https://doi.org/10.1080/16000870.2017.1330454
- Cramer, B. S., Toggweiler, J. R., Wright, J. D., Katz, M. E., & Miller, K. G. (2009). Ocean overturning since the Late
   Cretaceous: Inferences from a new benthic foraminiferal isotope compilation. *Paleoceanography*, 24(4).
   https://doi.org/10.1029/2008PA001683
- Cramer, B. S., Miller, K. G., Barrett, P. J., & Wright, J. D. (2011). Late Cretaceous–Neogene trends in deep ocean
   temperature and continental ice volume: Reconciling records of benthic foraminiferal geochemistry (δ<sup>18</sup>O
   and Mg/Ca) with sea level history. *Journal of Geophysical Research*, 116(C12), C12023.
   https://doi.org/10.1029/2011JC007255
- Cramwinckel, M. J., Huber, M., Kocken, I. J., Agnini, C., Bijl, P. K., Bohaty, S. M., et al. (2018). Synchronous tropical and polar temperature evolution in the Eocene. *Nature*, 559(7714), 382–386.
- 819 https://doi.org/10.1038/s41586-018-0272-2

820	Cramwinckel, M. J., Coxall, H. K., Śliwińska, K. K., Polling, M., Harper, D. T., Bijl, P. K., et al. (2020). A Warm,
821	Stratified, and Restricted Labrador Sea Across the Middle Eocene and Its Climatic Optimum.

822 Paleoceanography and Paleoclimatology, 35(10). https://doi.org/10.1029/2020PA003932

- Curry, W. B., & Oppo, D. W. (2005). Glacial water mass geometry and the distribution of δ13 C of ΣCO2 in the western Atlantic Ocean. *Paleoceanography*, 20(1). https://doi.org/10.1029/2004PA001021
- D'haenens, S., Bornemann, A., Claeys, P., Röhl, U., Steurbaut, E., & Speijer, R. P. (2014). A transient deep-sea
   circulation switch during Eocene Thermal Maximum 2. *Paleoceanography*, 29(5), 370–388.
   https://doi.org/10.1002/2013PA002567
- Donnadieu, Y., Pucéat, E., Moiroud, M., Guillocheau, F., & Deconinck, J.-F. (2016). A better-ventilated ocean triggered by Late Cretaceous changes in continental configuration. *Nature Communications*, 7(1), 10316. https://doi.org/10.1038/ncomms10316
- Döös, K., & Webb, D. J. (1994). The Deacon cell and the other meridional cells of the Southern Ocean. *Journal of Physical Oceanography*, 24(2), 429–442.
- Elsworth, G., Galbraith, E., Halverson, G., & Yang, S. (2017). Enhanced weathering and CO2 drawdown caused by latest Eocene strengthening of the Atlantic meridional overturning circulation. *Nature Geoscience*, 10(3), 213–216. https://doi.org/10.1038/ngeo2888
- 836 England, M. H., Hutchinson, D. K., Santoso, A., & Sijp, W. P. (2017). Ice–Atmosphere Feedbacks Dominate the 837 Response of the Climate System to Drake Passage Closure. *Journal of Climate*, *30*(15), 5775–5790. 838 https://doi.org/10.1175/JCLI-D-15-0554.1
- English, J. M., & Johnston, S. T. (2004). The Laramide Orogeny: What Were the Driving Forces? *International Geology Review*, *46*, 833–838.
- Fan, M., & Carrapa, B. (2014). Late Cretaceous-early Eocene Laramide uplift, exhumation, and basin subsidence in Wyoming: Crustal responses to flat slab subduction: Laramide uplift and exhumation. *Tectonics*, *33*(4), 509–529. https://doi.org/10.1002/2012TC003221
- Ferrari, R., Mashayek, A., McDougall, T. J., Nikurashin, M., & Campin, J.-M. (2016). Turning Ocean Mixing Upside
  Down. *Journal of Physical Oceanography*, *46*(7), 2239–2261. https://doi.org/10.1175/JPO-D-15-0244.1
- Ferreira, D., Cessi, P., Coxall, H. K., de Boer, A., Dijkstra, H. A., Drijfhout, S. S., et al. (2018). Atlantic-Pacific

  Asymmetry in Deep Water Formation. *Annual Review of Earth and Planetary Sciences*, *46*(1), 327–352.

  https://doi.org/10.1146/annurev-earth-082517-010045
- van de Flierdt, T., Griffiths, A. M., Lambelet, M., Little, S. H., Stichel, T., & Wilson, D. J. (2016). Neodymium in the oceans: a global database, a regional comparison and implications for palaeoceanographic research.

  Philosophical Transactions of the Royal Society A: Mathematical, Physical and Engineering Sciences,

  374(2081), 20150293. https://doi.org/10.1098/rsta.2015.0293
- Frank, M. (2002). Radiogenic isotopes: Tracers of past ocean circulation and erosional input. *Reviews of Geophysics*, *40*(1), 1001. https://doi.org/10.1029/2000RG000094
- Galbraith, E. D., Kwon, E. Y., Bianchi, D., Hain, M. P., & Sarmiento, J. L. (2015). The impact of atmospheric pCO<sub>2</sub> on carbon isotope ratios of the atmosphere and ocean. *Global Biogeochemical Cycles*, 29(3), 307–324. https://doi.org/10.1002/2014GB004929
- 618 Gleason, J. D., Thomas, D. J., Moore, T. C., Blum, J. D., Owen, R. M., & Haley, B. A. (2009). Early to middle Eocene history of the Arctic Ocean from Nd-Sr isotopes in fossil fish debris, Lomonosov Ridge. *Paleoceanography*, 24(2). https://doi.org/10.1029/2008PA001685

- Goldstein, S. L., & Hemming, S. R. (2014). Long-lived Isotopic Tracers in Oceanography, Paleoceanography, and Icesheet Dynamics. In *Treatise on Geochemistry* (pp. 453–483). Elsevier. https://doi.org/10.1016/B978-0-08-095975-7.00617-3
- Gordon, C., Gregory, J. M., & Wood, R. A. (2000). The simulation of SST, sea ice extents and ocean heat transports in a version of the Hadley Centre coupled model without flux adjustments, 16, 147–168.
- Green, J. A. M., & Huber, M. (2013). Tidal dissipation in the early Eocene and implications for ocean mixing: EOCENE TIDES. *Geophysical Research Letters*, 40(11), 2707–2713. https://doi.org/10.1002/grl.50510
- Gregg, M. C., Sanford, T. B., & Winkel, D. P. (2003). Reduced mixing from the breaking of internal waves in equatorial waters.

  Nature, 422(6931), 513–515. https://doi.org/10.1038/nature01507
- Guo, C., Bentsen, M., Bethke, I., Ilicak, M., Tjiputra, J., Toniazzo, T., et al. (2019). Description and evaluation of
   NorESM1-F: a fast version of the Norwegian Earth System Model (NorESM). Geoscientific Model
   Development, 12(1), 343–362. https://doi.org/10.5194/gmd-12-343-2019
- Hague, A. M., Thomas, D. J., Huber, M., Korty, R., Woodard, S. C., & Jones, L. B. (2012). Convection of North Pacific deep water during the early Cenozoic. *Geology*, *40*(6), 527–530. https://doi.org/10.1130/G32886.1
- Haley, B. A., Du, J., Abbott, A. N., & McManus, J. (2017). The Impact of Benthic Processes on Rare Earth Element
   and Neodymium Isotope Distributions in the Oceans. *Frontiers in Marine Science*, *4*, 426.
   https://doi.org/10.3389/fmars.2017.00426
- Harrington, G. J., Eberle, J., Le-Page, B. A., Dawson, M., & Hutchison, J. H. (2012). Arctic plant diversity in the Early
  Eocene greenhouse. *Proceedings of the Royal Society B: Biological Sciences*, *279*(1733), 1515–1521.

  https://doi.org/10.1098/rspb.2011.1704
- Hasumi, H. (2000). CCSR Ocean Component Model (COCO) Version 2.1, Tech. rep., The University of Tokyo.
- Herold, N., Buzan, J., Seton, M., Goldner, A., Green, J. A. M., Müller, R. D., et al. (2014). A suite of early Eocene (~ S5 Ma) climate model boundary conditions. *Geoscientific Model Development*, 7(5), 2077–2090. https://doi.org/10.5194/gmd-7-2077-2014
- Hilting, A. K., Kump, L. R., & Bralower, T. J. (2008). Variations in the oceanic vertical carbon isotope gradient and their implications for the Paleocene-Eocene biological pump. *Paleoceanography*, 23(3), PA3222. https://doi.org/10.1029/2007PA001458
- van Hinsbergen, D. J. J., de Groot, L. V., van Schaik, S. J., Spakman, W., Bijl, P. K., Sluijs, A., et al. (2015). A
   Paleolatitude Calculator for Paleoclimate Studies. *PLoS ONE*, *10*(6), e0126946.
   https://doi.org/10.1371/journal.pone.0126946
- Hohbein, M. W., Sexton, P. F., & Cartwright, J. A. (2012). Onset of North Atlantic Deep Water production coincident
   with inception of the Cenozoic global cooling trend. *Geology*, 40(3), 255–258.
   https://doi.org/10.1130/G32461.1
- Hollis, C. J., Handley, L., Crouch, E. M., Morgans, H. E. G., Baker, J. A., Creech, J., et al. (2009). Tropical sea temperatures in the high-latitude South Pacific during the Eocene. *Geology*, *37*(2), 99–102. https://doi.org/10.1130/G25200A.1
- Huber, M., & Sloan, L. C. (2001). Heat transport, deep waters, and thermal gradients: Coupled simulation of an
   Eocene greenhouse climate. *Geophysical Research Letters*, 28(18), 3481–3484.
   https://doi.org/10.1029/2001GL012943
- Huck, C. E., van de Flierdt, T., Bohaty, S. M., & Hammond, S. J. (2017). Antarctic climate, Southern Ocean circulation
   patterns, and deep water formation during the Eocene: Eocene Southern Ocean Circulation.
   *Paleoceanography*, 32(7), 674–691. https://doi.org/10.1002/2017PA003135

- Hutchinson, D. K., de Boer, A. M., Coxall, H. K., Caballero, R., Nilsson, J., & Baatsen, M. (2018). Climate sensitivity
   and meridional overturning circulation in the late Eocene using GFDL CM2.1. Climate of the Past, 14(6),
   789–810. https://doi.org/10.5194/cp-14-789-2018
- Hutchinson, D. K., Coxall, H. K., O'Regan, M., Nilsson, J., Caballero, R., & de Boer, A. M. (2019). Arctic closure as a
   trigger for Atlantic overturning at the Eocene-Oligocene Transition. *Nature Communications*, 10(1), 3797.
   https://doi.org/10.1038/s41467-019-11828-z
- Johns, W. E., Baringer, M. O., Beal, L. M., Cunningham, S. A., Kanzow, T., Bryden, H. L., et al. (2011). Continuous,
   Array-Based Estimates of Atlantic Ocean Heat Transport at 26.5°N. *Journal of Climate*, 24(10), 2429–2449.
   https://doi.org/10.1175/2010JCLI3997.1
- Kaminski, M. A., Berggren, W. A., & Gradstein, F. M. (1989). Paleogene benthic foraminifer biostratigraphy and
   paleoecology at Site 647, Southern Labrador Sea-CORE. Retrieved May 18, 2021, from
   https://core.ac.uk/display/1687161
- Kennedy-Asser, A. T., Lunt, D. J., Valdes, P. J., Ladant, J.-B., Frieling, J., & Lauretano, V. (2020). Changes in the high
   latitude Southern Hemisphere through the Eocene-Oligocene Transition: a model-data comparison.
   Climate of the Past. 16(2), 555–573. https://doi.org/10.5194/cp-16-555-2020Kroopnick, P. M. (1985). The
   distribution of <sup>13</sup>C of ΣCO2 in the world oceans. Deep Sea Research Part A. Oceanographic Research
   Papers, 32(1), 57–84. https://doi.org/10.1016/0198-0149(85)90017-2
- Ladant, J.-B., Donnadieu, Y., Bopp, L., Lear, C. H., & Wilson, P. A. (2018). Meridional Contrasts in Productivity
   Changes Driven by the Opening of Drake Passage. *Paleoceanography and Paleoclimatology*, 33(3), 302–317. https://doi.org/10.1002/2017PA003211re
- Large, W. G., McWilliams, J. C., & Doney, S. C. (1994). Oceanic vertical mixing: A review and a model with a nonlocal boundary layer parameterization. *Reviews of Geophysics*, *32*(4), 363. https://doi.org/10.1029/94RG01872
- Lauretano, V., Littler, K., Polling, M., Zachos, J. C., & Lourens, L. J. (2015). Frequency, magnitude and character of hyperthermal events at the onset of the Early Eocene Climatic Optimum. *Climate of the Past*, 11(10), 1313–1324. https://doi.org/10.5194/cp-11-1313-2015
- Lauretano, V., Hilgen, F. J., Zachos, J. C., & Lourens, L. J. (2016). Astronomically tuned age model for the early Eocene carbon isotope events: A new high-resolution  $\delta^{13}$ C benthic record of ODP Site 1263 between ~ 49 and ~ 54 Ma. Newsletters on Stratigraphy, 49(2), 383–400. https://doi.org/10.1127/nos/2016/0077de Lavergne, C., Madec, G., Roquet, F., Holmes, R. M., & McDougall, T. J. (2017). Abyssal ocean overturning shaped by seafloor distribution. *Nature*, 551(7679), 181–186. https://doi.org/10.1038/nature24472
- Ledwell, J. R., Montgomery, E. T., Polzin, K. L., St. Laurent, L. C., Schmitt, R. W., & Toole, J. M. (2000). Evidence for
   enhanced mixing over rough topography in the abyssal ocean. *Nature*, 403(6766), 179–182.
   https://doi.org/10.1038/35003164
- Littler, K., Röhl, U., Westerhold, T., & Zachos, J. C. (2014). A high-resolution benthic stable-isotope record for the
   South Atlantic: Implications for orbital-scale changes in Late Paleocene–Early Eocene climate and carbon cycling. Earth and Planetary Science Letters, 401, 18–30. https://doi.org/10.1016/j.epsl.2014.05.054
- Lumpkin, R., & Speer, K. (2007). Global ocean meridional overturning. Journal of Physical Oceanography, 37(10),
   2550–2562. https://doi.org/10.1175/JPO3130.1
- Lunt, D. J., Valdes, P. J., Jones, T. D., Ridgwell, A., Haywood, A. M., Schmidt, D. N., et al. (2010). CO2-driven ocean
   circulation changes as an amplifier of Paleocene-Eocene thermal maximum hydrate destabilization.
   *Geology*, 38(10), 875–878. https://doi.org/10.1130/G31184.1
- Lunt, D. J., Huber, M., Anagnostou, E., Baatsen, M. L. J., Caballero, R., DeConto, R., et al. (2017). The DeepMIP
   contribution to PMIP4: experimental design for model simulations of the EECO, PETM, and pre-PETM

946 947	(version 1.0). <i>Geoscientific Model Development, 10</i> (2), 889–901. https://doi.org/10.5194/gmd-10-889-2017
948 949 950	Lunt, D. J., Bragg, F., Chan, WL., Hutchinson, D. K., Ladant, JB., Niezgodzki, I., et al. (2021). <i>DeepMIP: Model intercomparison of early Eocene climatic optimum (EECO) large-scale climate features and comparison with proxy data</i> . <i>Climate of the Past</i> , 17(1), 203–227. https://doi.org/10.5194/cp-17-203-2021
951 952 953	Lynch-Stieglitz, J., Adkins, J. F., Curry, W. B., Dokken, T., Hall, I. R., Herguera, J. C., et al. (2007). Atlantic Meridional Overturning Circulation During the Last Glacial Maximum. <i>Science</i> , <i>316</i> (5821), 66–69. https://doi.org/10.1126/science.1137127
954 955 956	MacLeod, K. G., Isaza Londoño, C., Martin, E. E., Jiménez Berrocoso, Á., & Basak, C. (2011). Changes in North Atlantic circulation at the end of the Cretaceous ihouse interval. Nature Geoscience, 4(11), 779–782. https://doi.org/10.1038/ngeo1284
957 958	Maffre, P., Ladant, JB., Donnadieu, Y., Sepulchre, P., & Goddéris, Y. (2018). The influence of orography on modern ocean circulation. <i>Climate Dynamics</i> , 50(3–4), 1277–1289. https://doi.org/10.1007/s00382-017-3683-0
959 960 961 962 963 964	Markwick, P. J. (1998). Fossil crocodilians as indicators of Late Cretaceous and Cenozoic climates: implications for using palaeontological data in reconstructing palaeoclimate. <i>Palaeogeography, Palaeoclimatology, Palaeoecology, 137</i> (3–4), 205–271. https://doi.org/10.1016/S0031-0182(97)00108-9  Marsland, S. J., Haak, H., Jungclaus, J. H., Latif, M., and Roske, F. (2003). The Max-Planck-Institute global ocean/sea ice model with orthogonal curvilinear coordinates, Ocean Modelling, 5, 91–127, https://doi.org/10.1016/S1463-5003(02)00015-X
965 966 967	Marson, J. M., Myers, P. G., Hu, X., Petrie, B., Azetsu-Scott, K., & Lee, C. M. (2017). Cascading off the West Greenland Shelf: A numerical perspective. <i>Journal of Geophysical Research: Oceans</i> , 122(7), 5316–5328. https://doi.org/10.1002/2017JC012801
968 969	Martin, E. E., & Haley, B. A. (2000). Fossil fish teeth as proxies for seawater Sr and Nd isotopes. <i>Geochimica et Cosmochimica Acta</i> , <i>64</i> (5), 835–847. https://doi.org/10.1016/S0016-7037(99)00376-2
970 971 972	Martin, E. E., & Scher, H. D. (2004). Preservation of seawater Sr and Nd isotopes in fossil fish teeth: bad news and good news. <i>Earth and Planetary Science Letters</i> , 220(1–2), 25–39. https://doi.org/10.1016/S0012-821X(04)00030-5
973 974 975 976	McCarren, H., Thomas, E., Hasegawa, T., Röhl, U., & Zachos, J. C. (2008). Depth dependency of the Paleocene- Eocene carbon isotope excursion: Paired benthic and terrestrial biomarker records (Ocean Drilling Program Leg 208, Walvis Ridge). <i>Geochemistry, Geophysics, Geosystems</i> , 9(10), Q10008. https://doi.org/10.1029/2008GC002116
977 978 979 980	Miller, K. G., & Tucholke, B. E. (1983). Development of Cenozoic Abyssal Circulation South of the Greenland-Scotland Ridge. In M. H. P. Bott, S. Saxov, M. Talwani, & J. Thiede (Eds.), <i>Structure and Development of the Greenland-Scotland Ridge: New Methods and Concepts</i> (pp. 549–589). Boston, MA: Springer US. https://doi.org/10.1007/978-1-4613-3485-9 27

Msadek, R., Johns, W. E., Yeager, S. G., Danabasoglu, G., Delworth, T. L., & Rosati, A. (2013). The Atlantic

Meridional Heat Transport at 26.5°N and Its Relationship with the MOC in the RAPID Array and the GFDL

984

- and NCAR Coupled Models. *Journal of Climate*, *26*(12), 4335–4356. https://doi.org/10.1175/JCLI-D-12-00081.1
- 988 Munk, W., & Wunsch, C. (1998). Abyssal recipes II: Energetics of tidal and wind mixing. *Deep-Sea Research. Part I,*989 *Oceanographic Research Papers, 45*(12), 1977–2010.
- Munk, W. H. (1966). Abyssal recipes. In *Deep Sea Research and Oceanographic Abstracts* (Vol. 13, pp. 707–730).
   Citeseer.
- 992 Nikurashin, M., & Vallis, G. (2011). A Theory of Deep Stratification and Overturning Circulation in the Ocean.

  993 *Journal of Physical Oceanography*, *41*(3), 485–502. https://doi.org/10.1175/2010JPO4529.1
- Nisancioglu, K. H., Raymo, M. E., & Stone, P. H. (2003). Reorganization of Miocene deep water circulation in
   response to the shoaling of the Central American Seaway. *Paleoceanography*, *18*(1).
   https://doi.org/10.1029/2002PA000767
- Nong, G. T., Najjar, R. G., Seidov, D., & Peterson, W. H. (2000). Simulation of ocean temperature change due to the opening of Drake Passage. *Geophysical Research Letters*, *27*(17), 2689–2692.
   https://doi.org/10.1029/1999GL011072
- Nunes, F., & Norris, R. D. (2006). Abrupt reversal in ocean overturning during the Palaeocene/Eocene warm period.

  Nature, 439(7072), 60–63. https://doi.org/10.1038/nature04386
- Omta, A. W., & Dijkstra, H. A. (2003). A physical mechanism for the Atlantic–Pacific flow reversal in the early
  Miocene. *Global and Planetary Change*, *36*(4), 265–276. https://doi.org/10.1016/S0921-8181(02)00221-7
- O'Regan, M., Williams, C., Frey, K., & Jakobsson, M. (2011). A Synthesis of the Long-Term Paleoclimatic Evolution of the Arctic. *Oceanography*, 24(3), 66–80. https://doi.org/10.5670/oceanog.2011.57
- Orsi, A. H., Johnson, G. C., & Bullister, J. L. (1999). Circulation, mixing, and production of Antarctic Bottom Water.
  Progress in Oceanography, 43(1), 55–109. https://doi.org/10.1016/S0079-6611(99)00004-X
- Pacanowski, R. C., & Philander, S. G. H. (1981). Parameterization of vertical mixing in numerical models of tropical oceans. *Journal of Physical Oceanography*, *11*(11), 1443–1451.
- Pak, D. K., & Miller, K. G. (1992). Paleocene to Eocene benthic foraminiferal isotopes and assemblages: Implications for deepwater circulation. *Paleoceanography*, 7(4), 405–422. https://doi.org/10.1029/92PA01234
- Pross, J., Contreras, L., Bijl, P. K., Greenwood, D. R., Bohaty, S. M., Schouten, S., et al. (2012). Persistent neartropical warmth on the Antarctic continent during the early Eocene epoch. *Nature*, *488*(7409), 73–77. https://doi.org/10.1038/nature11300
- 1015 Roberts, C. D., LeGrande, A. N., & Tripati, A. K. (2009). Climate sensitivity to Arctic seaway restriction during the
  1016 early Paleogene. *Earth and Planetary Science Letters*, 286(3–4), 576–585.
  1017 https://doi.org/10.1016/j.epsl.2009.07.026
- 1018 Robinson, SA., Murphy, D. P., Vance, D., & Thomas, D. J. (2010). Formation of "Southern Component Water" in the
  1019 Late Cretaceous: Evidence from Nd-isotopes. *Geology*, *38*(10), 871–874.
  1020 https://doi.org/10.1130/G31165.1
- 1021 Robinson, Suzanne, Ivanovic, R., van de Flierdt, T., Blanchet, C. L., Tachikawa, K., Martin, E. E., et al. (2021). Global
  1022 continental and marine detrital εNd: An updated compilation for use in understanding marine Nd cycling.
  1023 *Chemical Geology*, *567*, 120119. https://doi.org/10.1016/j.chemgeo.2021.120119
- 1024 Rose, B. E. J., & Ferreira, D. (2013). Ocean Heat Transport and Water Vapor Greenhouse in a Warm Equable
  1025 Climate: A New Look at the Low Gradient Paradox. *Journal of Climate*, 26(6), 2117–2136.
  1026 https://doi.org/10.1175/JCLI-D-11-00547.1

- Scher, H. D., & Martin, E. E. (2004). Circulation in the Southern Ocean during the Paleogene inferred from neodymium isotopes. *Earth and Planetary Science Letters*, 228(3–4), 391–405.
   https://doi.org/10.1016/j.epsl.2004.10.016
- Sepulchre, P., Caubel, A., Ladant, J.-B., Bopp, L., Boucher, O., Braconnot, P., et al. (2020). IPSL-CM5A2 an Earth system model designed for multi-millennial climate simulations. Geosci. Model Dev., 13, 3011–3053, https://doi.org/10.5194/gmd-13-3011-2020
- Sexton, P. F., Wilson, P. A., & Norris, R. D. (2006). Testing the Cenozoic multisite composite  $\delta^{18}$ O and  $\delta^{13}$ C curves:

  New monospecific Eocene records from a single locality, Demerara Rise (Ocean Drilling Program Leg 207).

  Paleoceanography, 21(2). https://doi.org/10.1029/2005PA001253
- Sexton, P. F., Wilson, P. A., & Pearson, P. N. (2006b). Microstructural and geochemical perspectives on planktic foraminiferal preservation: "Glassy" versus "Frosty." *Geochemistry, Geophysics, Geosystems,* 7(12), Q12P19. https://doi.org/10.1029/2006GC001291
- Sexton, P. F., Norris, R. D., Wilson, P. A., Pälike, H., Westerhold, T., Röhl, U., et al. (2011). Eocene global warming events driven by ventilation of oceanic dissolved organic carbon. *Nature*, 471(7338), 349–352. https://doi.org/10.1038/nature09826
- Sherwood, S. C., Webb, M. J., Annan, J. D., Armour, K. C., Forster, P. M., Hargreaves, J. C., et al. (2020). An

  Assessment of Earth's Climate Sensitivity Using Multiple Lines of Evidence. *Reviews of Geophysics*, *58*(4).

  https://doi.org/10.1029/2019RG000678
- Simmons, H. L., Jayne, S. R., Laurent, L. C. S., & Weaver, A. J. (2004). Tidally driven mixing in a numerical model of the ocean general circulation, Ocean Model., 6, 245–263, https://doi.org/10.1016/S1463-5003(03)00011-047
- 1048 Smith, R., Jones, P., Briegleb, B., Bryan, F., Danabasoglu, G., Dennis, J., et al. (2010). The parallel ocean program
  1049 (POP) reference manual ocean component of the community climate system model (CCSM) and
  1050 community earth system model (CESM), Rep. LAUR-01853, 141, 1–140.
- Stap, L., Lourens, L. J., Thomas, E., Sluijs, A., Bohaty, S., & Zachos, J. C. (2010). High-resolution deep-sea carbon and
   oxygen isotope records of Eocene Thermal Maximum 2 and H2. *Geology*, 38(7), 607–610.
   https://doi.org/10.1130/G30777.1
- Stärz, M., Jokat, W., Knorr, G., & Lohmann, G. (2017). Threshold in North Atlantic-Arctic Ocean circulation
   controlled by the subsidence of the Greenland-Scotland Ridge. *Nature Communications*, 8(1), 15681.
   https://doi.org/10.1038/ncomms15681
- Stommel, H., & Arons, A. B. (1960). On the abyssal circulation of the world ocean—I. Stationary planetary flow patterns on a sphere. Deep Sea Research (1953), 6, 140–154. https://doi.org/10.1016/0146-6313(59)90065-6
- Tachikawa, K., Athias, V., & Jeandel, C. (2003). Neodymium budget in the modern ocean and paleo-oceanographic implications. *Journal of Geophysical Research*, *108*(C8), 3254. https://doi.org/10.1029/1999JC000285
- Thomas, D. J. (2004). Evidence for deep-water production in the North Pacific Ocean during the early Cenozoic warm interval. *Nature*, *430*(6995), 65–68. https://doi.org/10.1038/nature02639
- Thomas, D. J., Bralower, T. J., & Jones, C. E. (2003). Neodymium isotopic reconstruction of late Paleocene–early
   Eocene thermohaline circulation. *Earth and Planetary Science Letters*, 209(3–4), 309–322.
   https://doi.org/10.1016/S0012-821X(03)00096-7
- Thomas, D. J., Lyle, M., Moore, T. C., & Rea, D. K. (2008). Paleogene deepwater mass composition of the tropical Pacific and implications for thermohaline circulation in a greenhouse world. *Geochemistry, Geophysics, Geosystems*, 9(2), 1-13. https://doi.org/10.1029/2007GC001748

- Thomas, D. J., Korty, R., Huber, M., Schubert, J. A., & Haines, B. (2014). Nd isotopic structure of the Pacific Ocean
   70-30 Ma and numerical evidence for vigorous ocean circulation and ocean heat transport in a
   greenhouse world. *Paleoceanography*, 29(5), 454–469. https://doi.org/10.1002/2013PA002535
- Tierney, J. E., Poulsen, C. J., Montañez, I. P., Bhattacharya, T., Feng, R., Ford, H. L., et al. (2020). Past climates inform our future. *Science*, 370(6517), eaay3701. https://doi.org/10.1126/science.aay3701
- Toggweiler, J. R., & Bjornsson, H. (2000). Drake Passage and palaeoclimate. *Journal of Quaternary Science*, *15*, 319– 328.
- Toumoulin, A., Donnadieu, Y., Ladant, J. -B., Batenburg, S. J., Poblete, F., & Dupont-Nivet, G. (2020). Quantifying the Effect of the Drake Passage Opening on the Eocene Ocean. *Paleoceanography and Paleoclimatology*, 35(8). https://doi.org/10.1029/2020PA003889
- Trenberth, K. E., & Caron, J. M. (2001). Estimates of Meridional Atmosphere and Ocean Heat Transports. *Journal of Climate*, *14*, 3433–3443.
- Utescher, T., & Mosbrugger, V. (2007). Eocene vegetation patterns reconstructed from plant diversity A global
   perspective. *Palaeogeography, Palaeoclimatology, Palaeoecology, 247*(3–4), 243–271.
   https://doi.org/10.1016/j.palaeo.2006.10.022
- Vahlenkamp, M., Niezgodzki, I., De Vleeschouwer, D., Lohmann, G., Bickert, T., & Pälike, H. (2018). Ocean and
   climate response to North Atlantic seaway changes at the onset of long-term Eocene cooling. *Earth and Planetary Science Letters*, 498, 185–195. https://doi.org/10.1016/j.epsl.2018.06.031
- Valdes, P. J., Armstrong, E., Badger, M. P. S., Bradshaw, C. D., Bragg, F., Crucifix, M., et al. (2017). The BRIDGE
   HadCM3 family of climate models: HadCM3@Bristol v1.0. Geoscientific Model Development, 10(10),
   3715–3743. https://doi.org/10.5194/gmd-10-3715-2017
- 1091 Via, R. K., & Thomas, D. J. (2006). Evolution of Atlantic thermohaline circulation: Early Oligocene onset of deep-1092 water production in the North Atlantic. *Geology*, *34*(6), 441. https://doi.org/10.1130/G22545.1
- Voigt, S., Jung, C., Friedrich, O., Frank, M., Teschner, C., & Hoffmann, J. (2013). Tectonically restricted deep-ocean
   circulation at the end of the Cretaceous greenhouse. *Earth and Planetary Science Letters*, 369–370, 169–
   177. https://doi.org/10.1016/j.epsl.2013.03.019
- Westerhold, T., Röhl, U., Donner, B., & Zachos, J. C. (2018). Global Extent of Early Eocene Hyperthermal Events: A
   New Pacific Benthic Foraminiferal Isotope Record From Shatsky Rise (ODP Site 1209). *Paleoceanography* and Paleoclimatology, 33(6), 626–642. https://doi.org/10.1029/2017PA003306
- Westerhold, Thomas, Röhl, U., Donner, B., McCarren, H. K., & Zachos, J. C. (2011). A complete high-resolution
   Paleocene benthic stable isotope record for the central Pacific (ODP Site 1209). *Paleoceanography*, 26(2).
   https://doi.org/10.1029/2010PA002092
- Westerhold, T., Marwan, N., Drury, A. J., Liebrand, D., Agnini, C., Anagnostou, E., et al. (2020). An astronomically
   dated record of Earth's climate and its predictability over the last 66 million years. *Science*, *369*(6509),
   1383–1387. https://doi.org/10.1126/science.aba6853
- Wilson, J. D., Monteiro, F. M., Schmidt, D. N., Ward, B. A., & Ridgwell, A. (2018). Linking Marine Plankton
   Ecosystems and Climate: A New Modeling Approach to the Warm Early Eccene Climate.
   Paleoceanography and Paleoclimatology, 33(12), 1439–1452. https://doi.org/10.1029/2018PA003374
- Winguth, A. M. E., Thomas, E., & Winguth, C. (2012). Global decline in ocean ventilation, oxygenation, and
   productivity during the Paleocene-Eocene Thermal Maximum: Implications for the benthic extinction.
   Geology, 40(3), 263–266. https://doi.org/10.1130/G32529.1

1111 1112 1113 1114	<ul> <li>Wolfe, C. L., &amp; Cessi, P. (2011). The Adiabatic Pole-to-Pole Overturning Circulation. <i>Journal of Physical Oceanography</i>, 41(9), 1795–1810. https://doi.org/10.1175/2011JPO4570.1</li> <li>Wolfe, C. L., &amp; Cessi, P. (2014). Salt Feedback in the Adiabatic Overturning Circulation. <i>Journal of Physical Oceanography</i>, 44(4), 1175–1194. https://doi.org/10.1175/JPO-D-13-0154.1</li> </ul>
1115 1116	Yang, S., Galbraith, E., & Palter, J. (2014). Coupled climate impacts of the Drake Passage and the Panama Seaway. Climate Dynamics, 43(1–2), 37–52. https://doi.org/10.1007/s00382-013-1809-6
1117 1118	Zachos, J. (2001). Trends, Rhythms, and Aberrations in Global Climate 65 Ma to Present. <i>Science</i> , 292(5517), 686–693. https://doi.org/10.1126/science.1059412
1119 1120 1121	Zaucker, F., Stocker, T. F., & Broecker, W. S. (1994). Atmospheric freshwater fluxes and their effect on the global thermohaline circulation. <i>Journal of Geophysical Research</i> , <i>99</i> (C6), 12443. https://doi.org/10.1029/94JC00526
1122 1123 1124	Zhang, X., Prange, M., Steph, S., Butzin, M., Krebs, U., Lunt, D. J., et al. (2012). Changes in equatorial Pacific thermocline depth in response to Panamanian seaway closure: Insights from a multi-model study. <i>Earth and Planetary Science Letters</i> , 317–318, 76–84. https://doi.org/10.1016/j.epsl.2011.11.028
1125 1126 1127	Zhang, Y., Huck, T., Lique, C., Donnadieu, Y., Ladant, JB., Rabineau, M., & Aslanian, D. (2020). Early Eocene vigorous ocean overturning and its contribution to a warm Southern Ocean. <i>Climate of the Past</i> , <i>16</i> (4), 1263–1283. https://doi.org/10.5194/cp-16-1263-2020
1128 1129 1130	Zhang, Y., Grima, N., & Huck, T. (2021). Fates of Paleo - Antarctic Bottom Water During the Early Eocene: Based on a Lagrangian Analysis of IPSL - CM5A2 Climate Model Simulations. <i>Paleoceanography and Paleoclimatology</i> , 36(1). https://doi.org/10.1029/2019PA003845
1131 1132	Zhu, J., Poulsen, C. J., & Tierney, J. E. (2019). Simulation of Eocene extreme warmth and high climate sensitivity through cloud feedbacks. <i>Science Advances</i> , <i>5</i> (9), eaax1874. https://doi.org/10.1126/sciadv.aax1874

## 1134 Figures

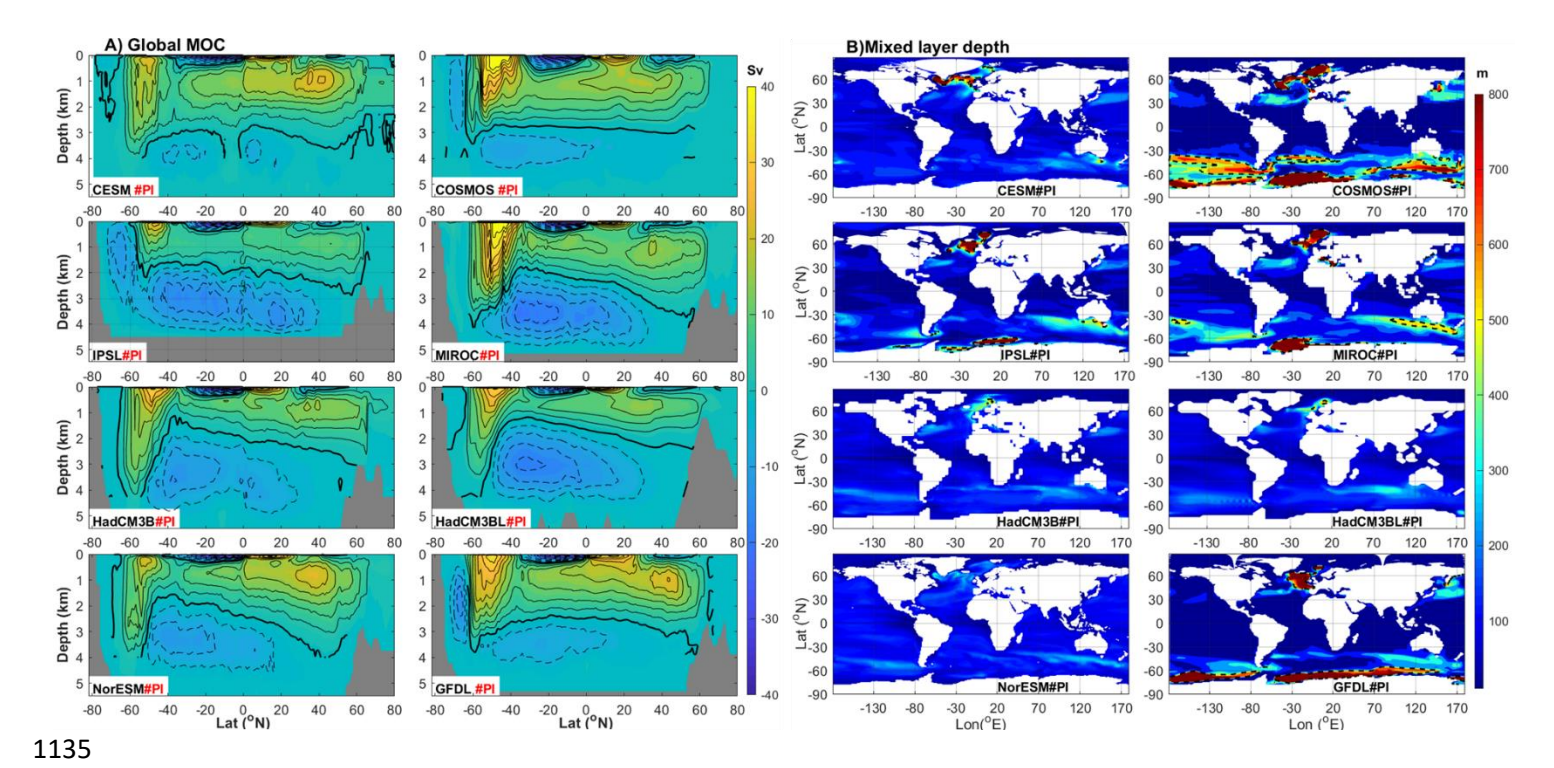


**Fig. 1** A) Global meridional overturning circulation(MOC), showing overturning streamfunction in the unit of Sverdrups (Sv, contour interval: 4 Sv) for the pre-industrial simulations (PI-1x), consisting of the NADW (positive values indicate clockwise circulation using solid lines) and Antarctic bottom waters AABW (negative values indicate anticlockwise circulation using dashed lines, and the zero contour is bold). B) maximum mixed layer depth (MLD, in m), indicative of deepwater formation sites. Dashed lines mark 500 m contour.

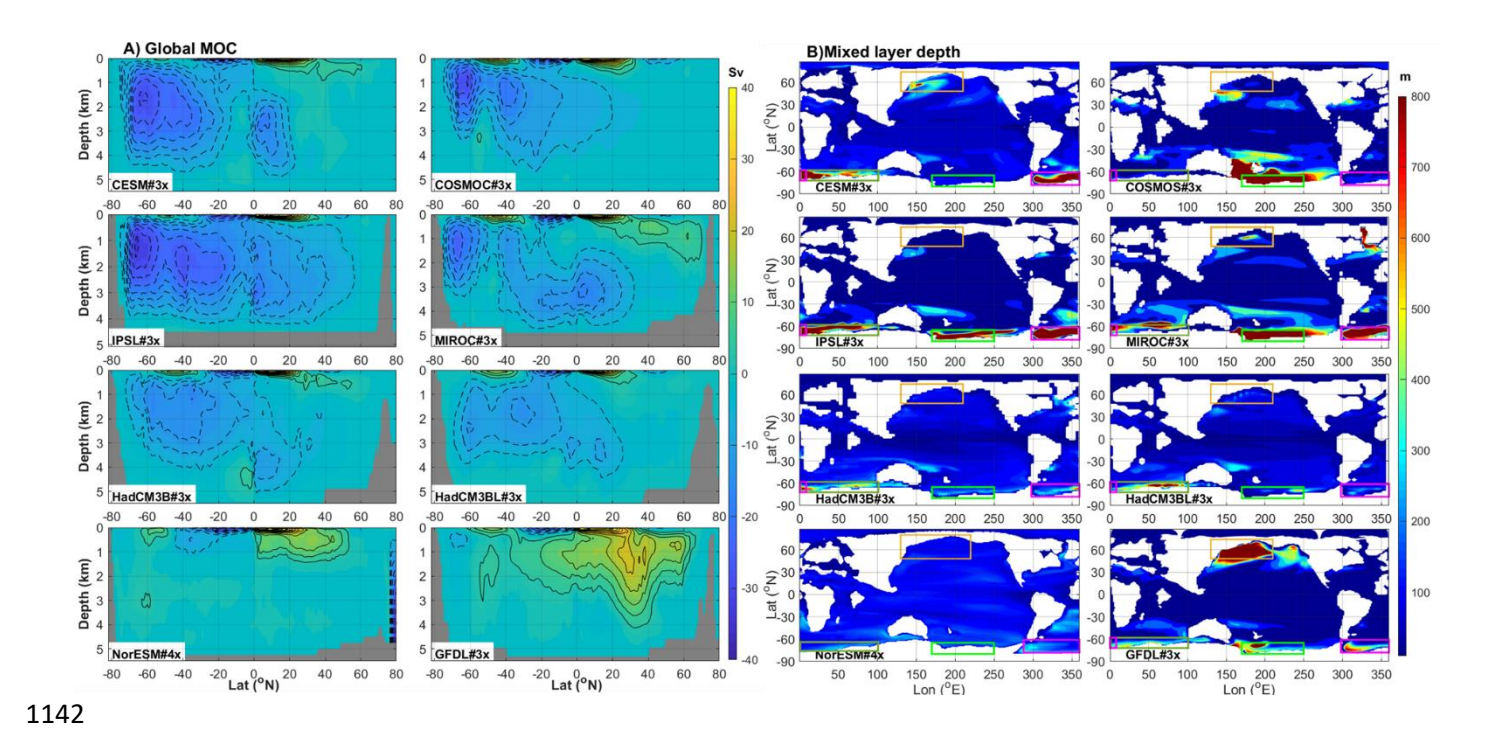


**Fig. 2** A) Global meridional overturning circulation (MOC) (contour interval: 4 Sv) showing mostly anticlockwise overturning circulation, and B) mixed layer depth (MLD) (m) for the Eocene-3x(4x) simulations. Colored boxes indicate regions used in the freshwater calculation.

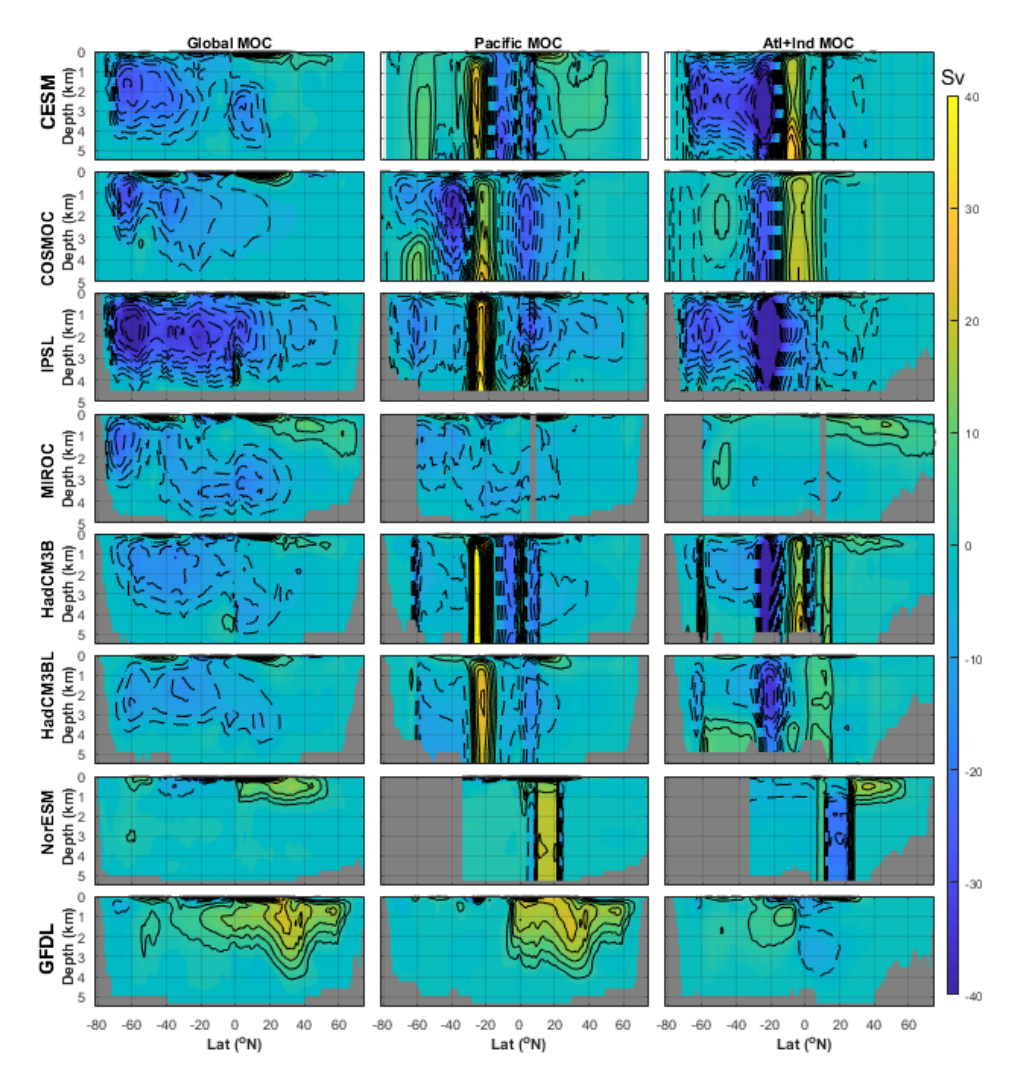


**Fig. 3** Separation of AMOC and PMOC from the global MOC in Eocene-3x simulations to show overturning circulation in two basins. Large values in the tropics indicate inter-basin exchanges, and a northward shift of these values in NorESM likely due to their more north tropical gateway that probably relate to their paleomagnetic reference bathymetry frame. NB, AMOC and PMOC in the CESM, COSMOS, IPSL and MIROC models are calculated offline.

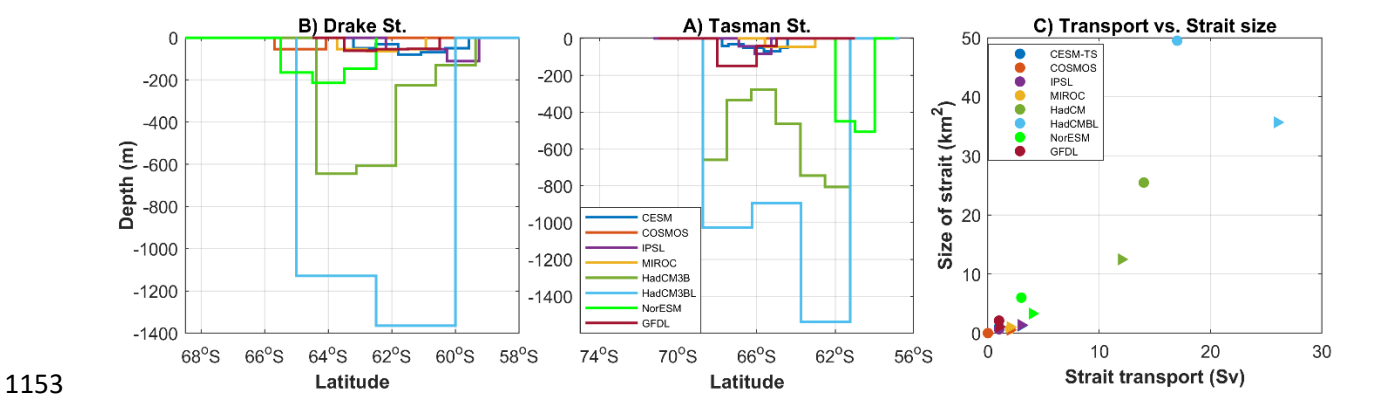


**Fig. 4** Drake Passage and Tasman strait configuration and their relationship to water mass transport. Depth-latitude profile of Drake Passage (A) at round 300°E, and B) Tasman Strait at 150°E. C) Scatter plot of water volume transport (Sv) through straits versus size of high-latitude straits (in km², width\*depth). Triangles and circles indicate the Tasman Gateway and Drake Passage.

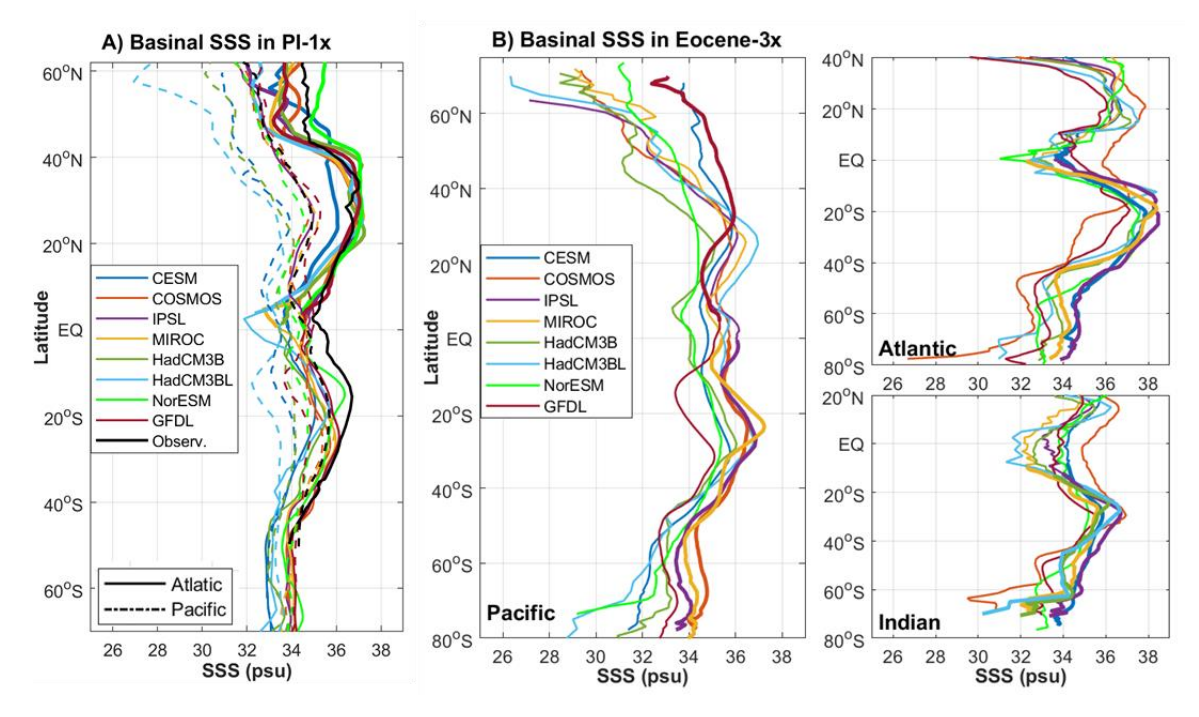


**Fig. 5 A)** Zonal mean sea-surface salinity (SSS) on a basin scale in the pre-industrial (PI-1x) simulations and compared with observations (black, redrawn from Ferreira et al., 2018). Deepwater formation in the Atlantic is highlighted by thickened lines. **B)** Simulated zonal mean (basin scale) SSS for the early Eocene, with thick lines indicating deep convection in the respective basins. Basin boundaries are set at the similar longitudes as the present-day. Note: Zonal mean SSS of the CESM simulation was homogeneously reduced by 0.7 psu, given its more saline initial condition compared with other models.

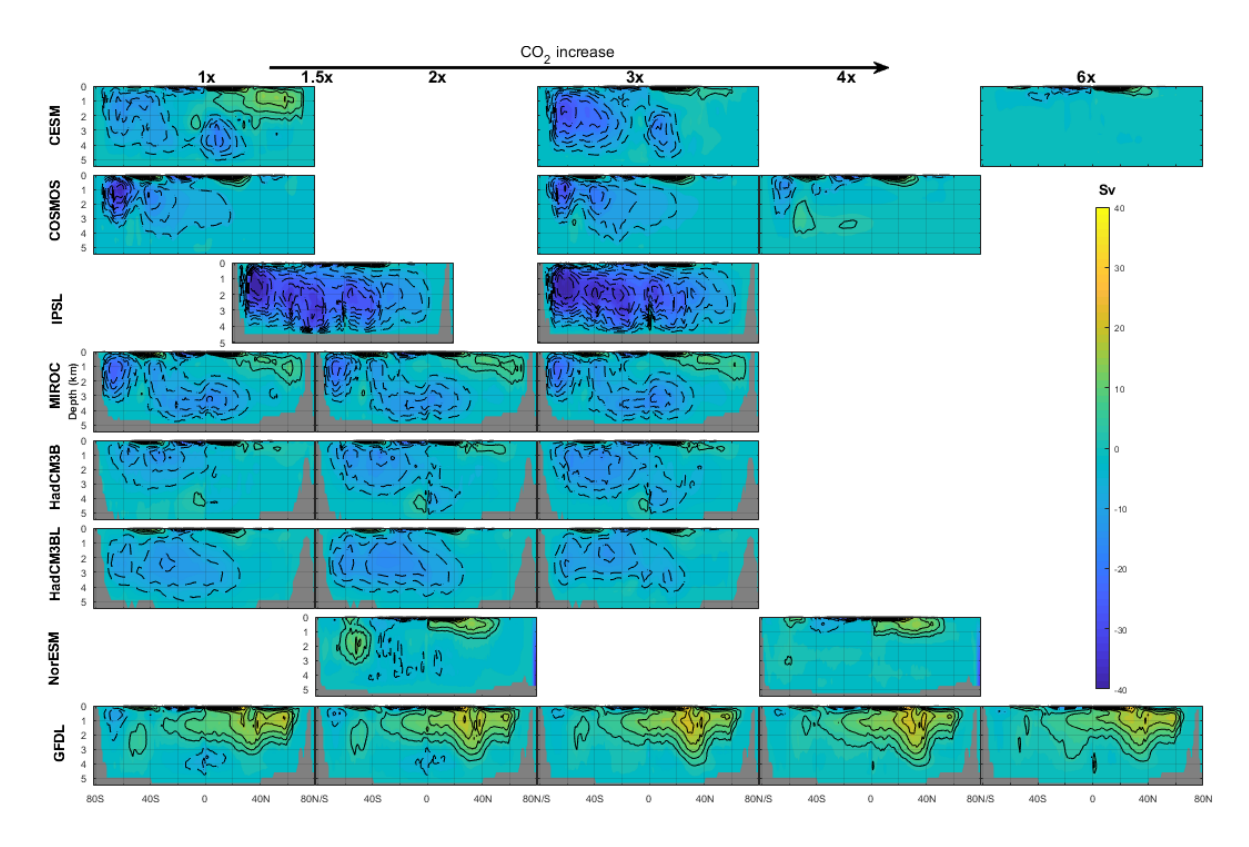


**Fig. 6** Global meridional overturning circulation (MOC, in Sv) response to atmospheric  $CO_2$  concentrations. The global MOC results from the IPSL simulation include tidal mixing (M2), because the 1.5x simulation is only run with M2. This tidal mixing contributes 7 Sv to the MOC, without changing its structure, as shown in Fig. 2A.

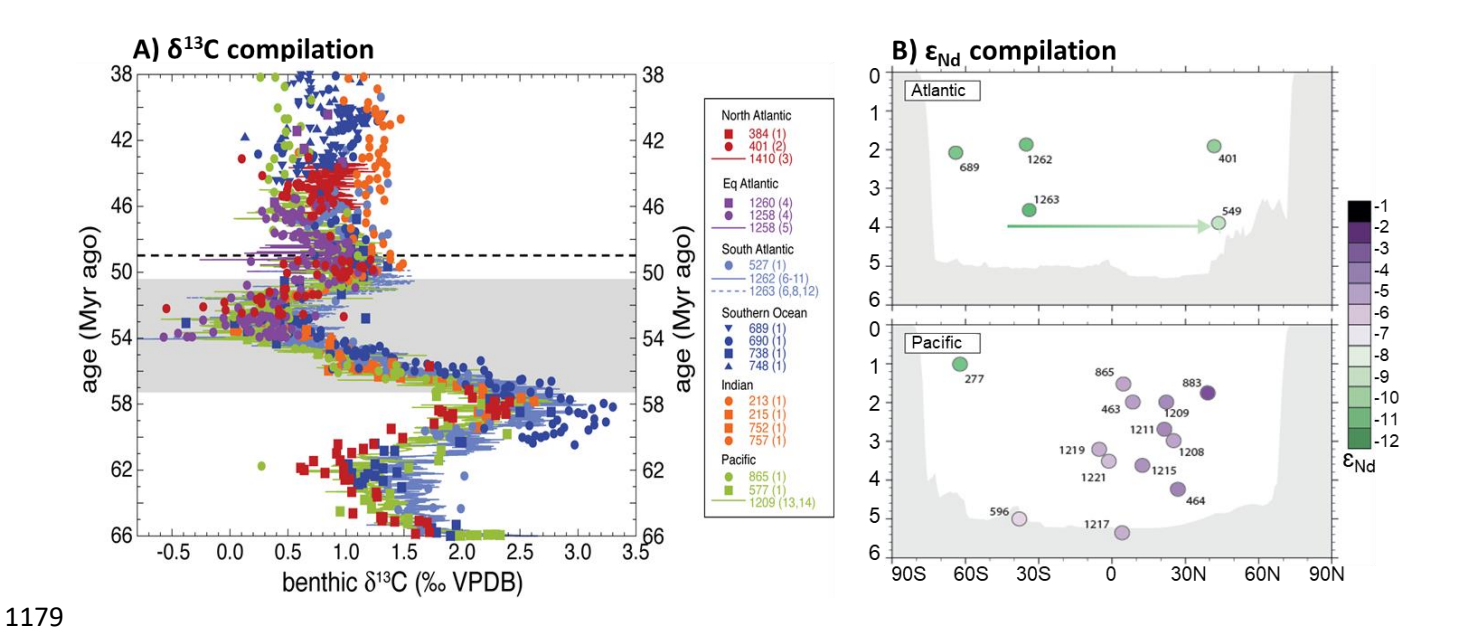


**Fig. 7** Proxy-based ocean circulation. A) Deep sea (benthic foraminifera)  $\delta^{13}$ C compilation through the Palaeocene and Eocene from deep sea drilling sites (~1500 to 3500 m paleo-water depth), grouped by geographical region (ocean basin). Grey shaded bar denotes interval of diminished benthic  $\delta^{13}$ C differences between ocean basins, that approximately corresponds to the early Eocene. Dashed line marks the timing of onset of the progressive Cenozoic global cooling trend. Ages for all datasets are converted to the new calibration of the geomagnetic polarity timescale (Westerhold et al., 2020). Data sources numbered in the figure legend are: (1) Zachos et al. (2001), (2) Bornemann et al. (2016), (3) Vahlenkamp et al. (2018), (4) Sexton et al., (2006), (5) Sexton et al. (2011), (6) Lauretano et al. (2015), (7) Littler et al. (2014), (8) Stap et al. (2010), (9) McCarren et al. (2008), (10) Barnet et al. (2019), (11) Barnet et al. (2018), (12) Lauretano et al. (2016), (13) Westerhold et al. (2018), (14) Westerhold et al. (2011). B) compilation of neodymium (Nd) isotope signatures as a function of depth and latitude covering the time window from 54 to 45 Ma in the Atlantic (omitting marginal sites 1001, 1258 and 1261) and Pacific (omitting marginal sites 1171 and 1172). Arrows indicate potential direction of water-mass movement. Mean basin bathymetry from Herold et al. (2014).

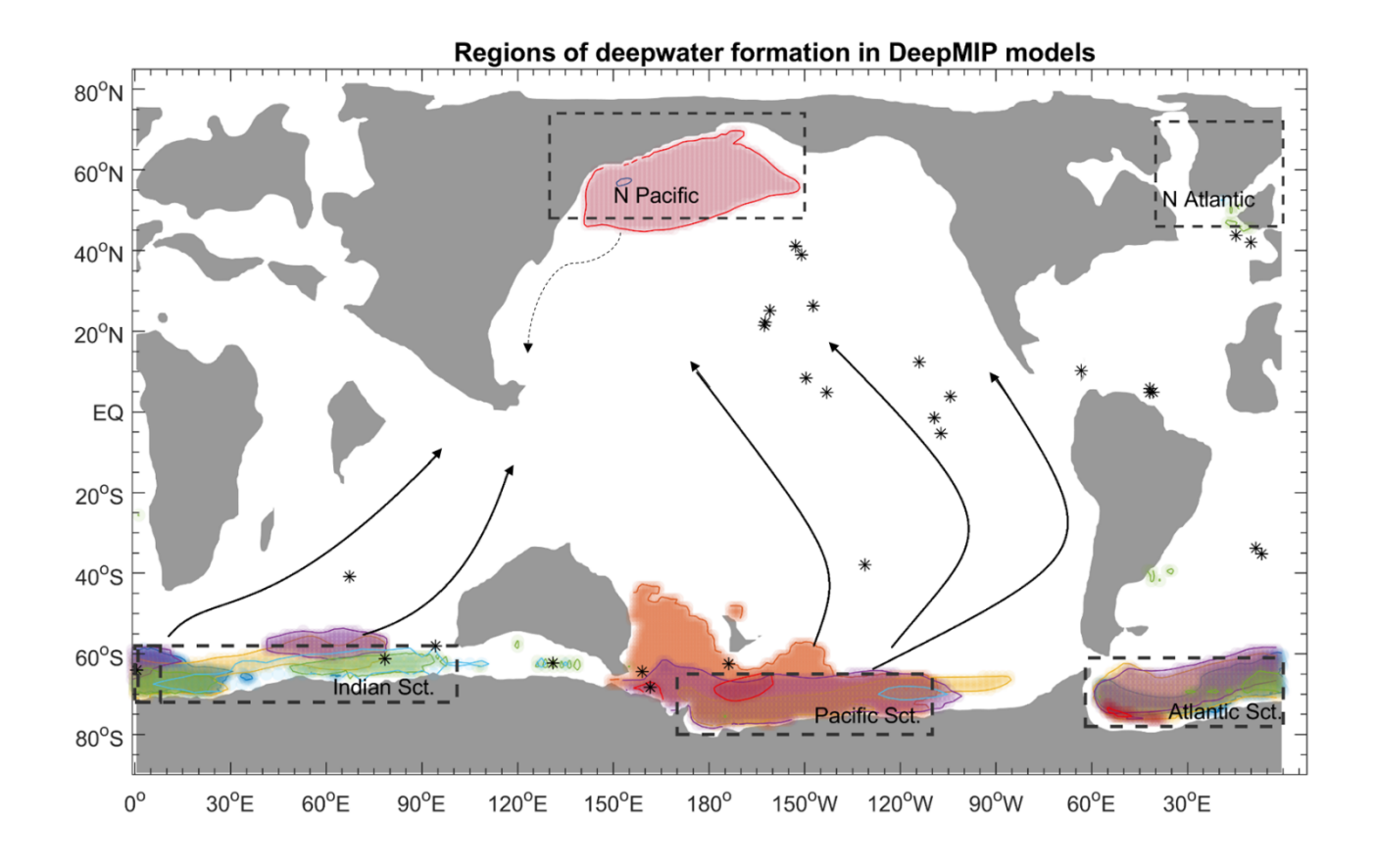


**Fig. 8** Regions of deep water formed in DeepMIP models, as revealed by deep mixed layer depth (model-specific colored-filled contour fields). Dashed boxes emphasize high-latitude basins where deepwater may form in the models. Most models suggest deepwater formed in the Southern Ocean, indicating this is a likely feature of the early Eocene; only the GFDL model shows deepwater formation in the North Pacific, thus the question of sinking there remains less certain. No model indicates deep water formeing in the North Atlantic during the early Eocene. Arrows schematically illustrate the pathway of the Southern Ocean deep water. Stars mark the sites of Nd measurements.

Table 1. Freshwater flux(m/yr) into the ocean from the atmosphere for regions marked in Figure. 2B.
 Shaded cells indicate the regions where deepwater formation occurs.

		Northern	Hemisphere		Southern Oce	an 1217
		N. Pacific	N. Atlantic	S. Pacific	S. Atlantic	Atlantic+Indian
CESM	(3x)	0.6346	1.0423	0.7080	0.5945	0.810 <sup>1</sup> / <sub>7</sub> 218
CESIVI	(1x)	0.6491	0.3393	0.4418	0.4310	0.6107 <sub>219</sub>
COSMO	<b>OS</b> (3x)	1.5323	2.5472	0.8282	1.0550	1.1133
IPSL- CM5A2(3x)		1.08	1.0780	0.574	0.459	0.646
MIROC(3x)		1.1591	0.8505	0.4510	0.4289	0.5868
HadCN	<b>13B</b> (3x)	1.0786	1.2150	0.5912	0.6122	0.7760
HadCN	<b>13BL</b> (3x)	1.1346	1.1865	0.6687	0.7052	0.8389
NorESN	<b>√</b> 1(4x)	0.8024	0.3368	1.0545	0.5450	0.6665 1224
CEDI	(3x)	0.5078	1.3791	0.5667	0.7024	0.7611
GFDL	(1x)	0.3663	1.1617	0.3487	0.4456	0.488 <b>9</b> 225

Figure1.		

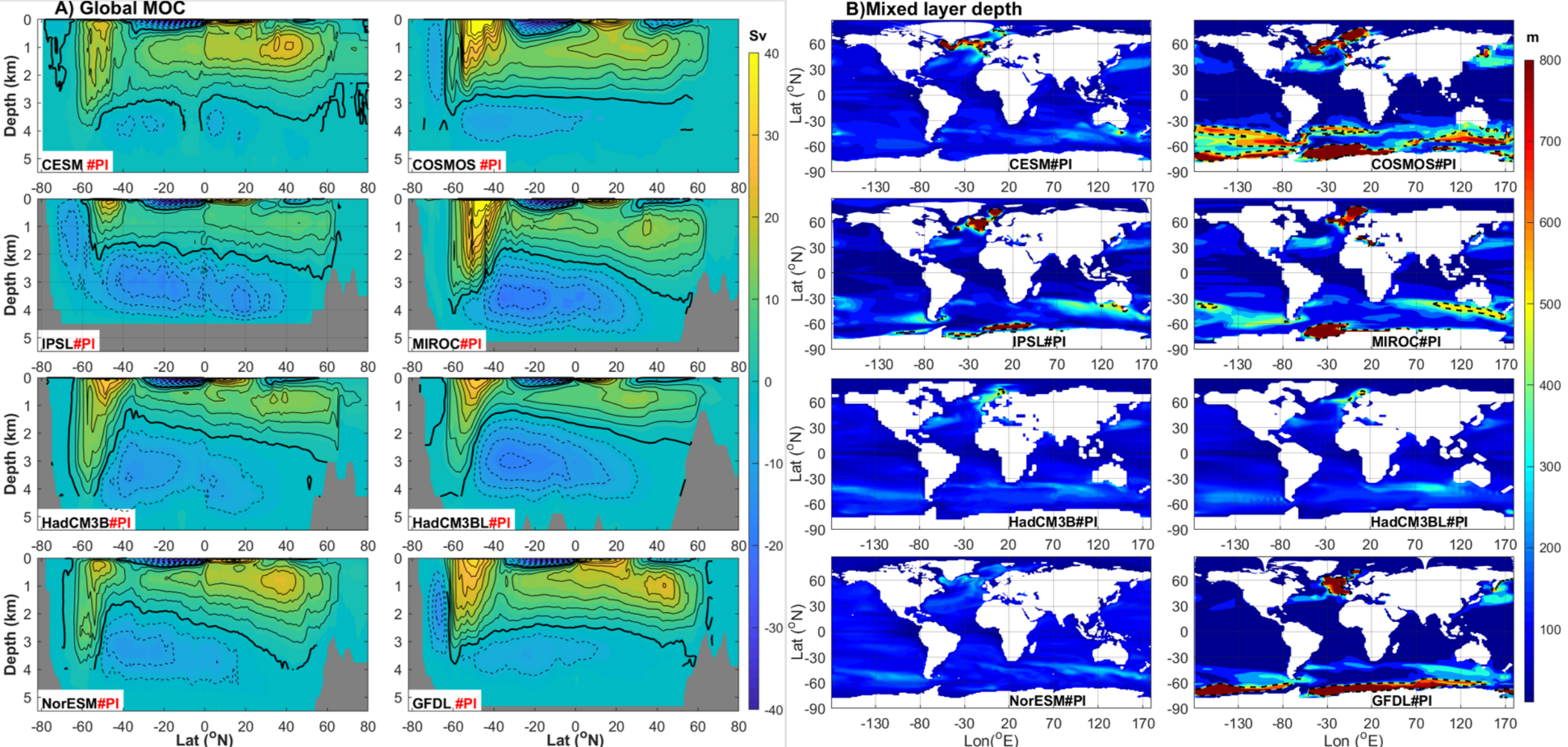


Figure2.	

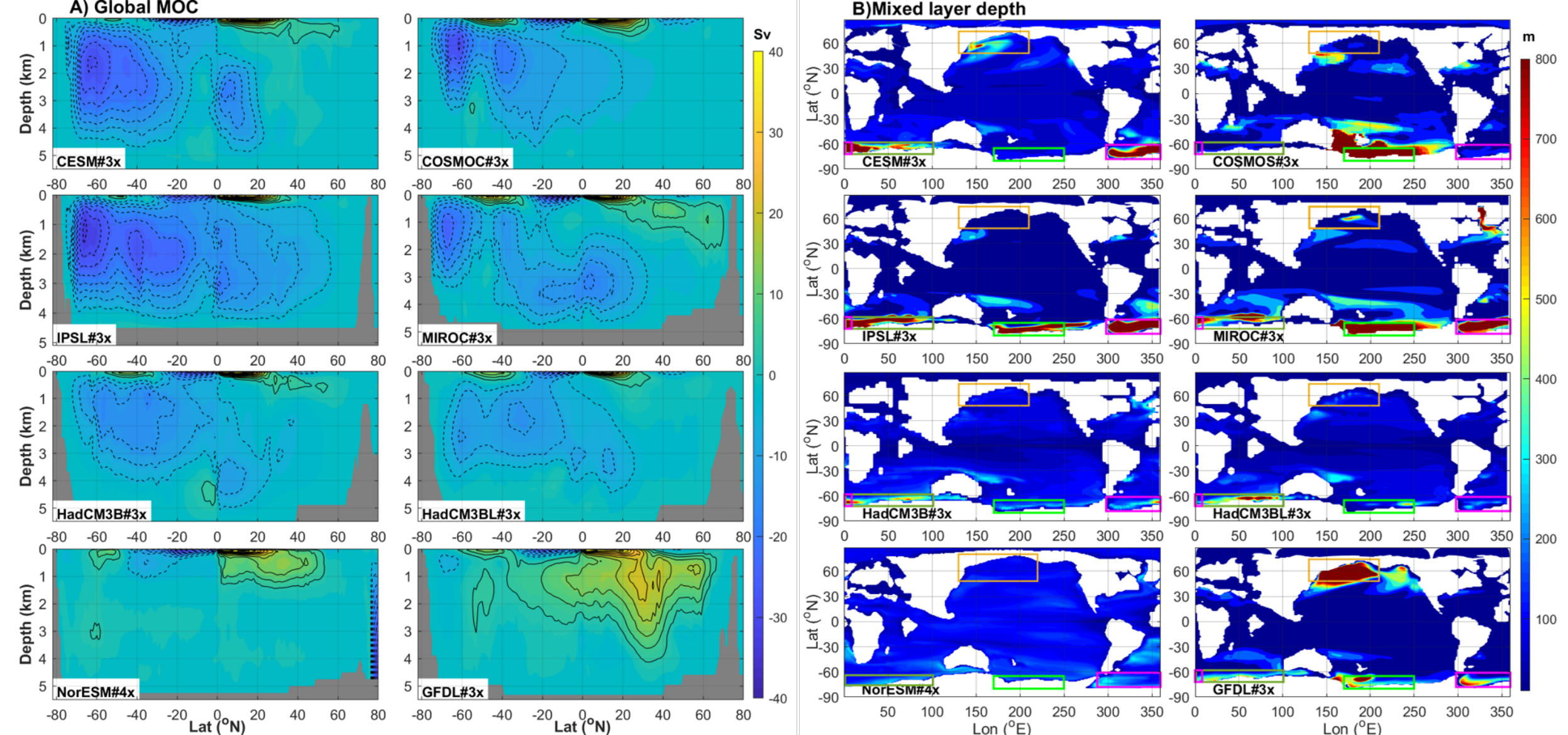


Figure3.			

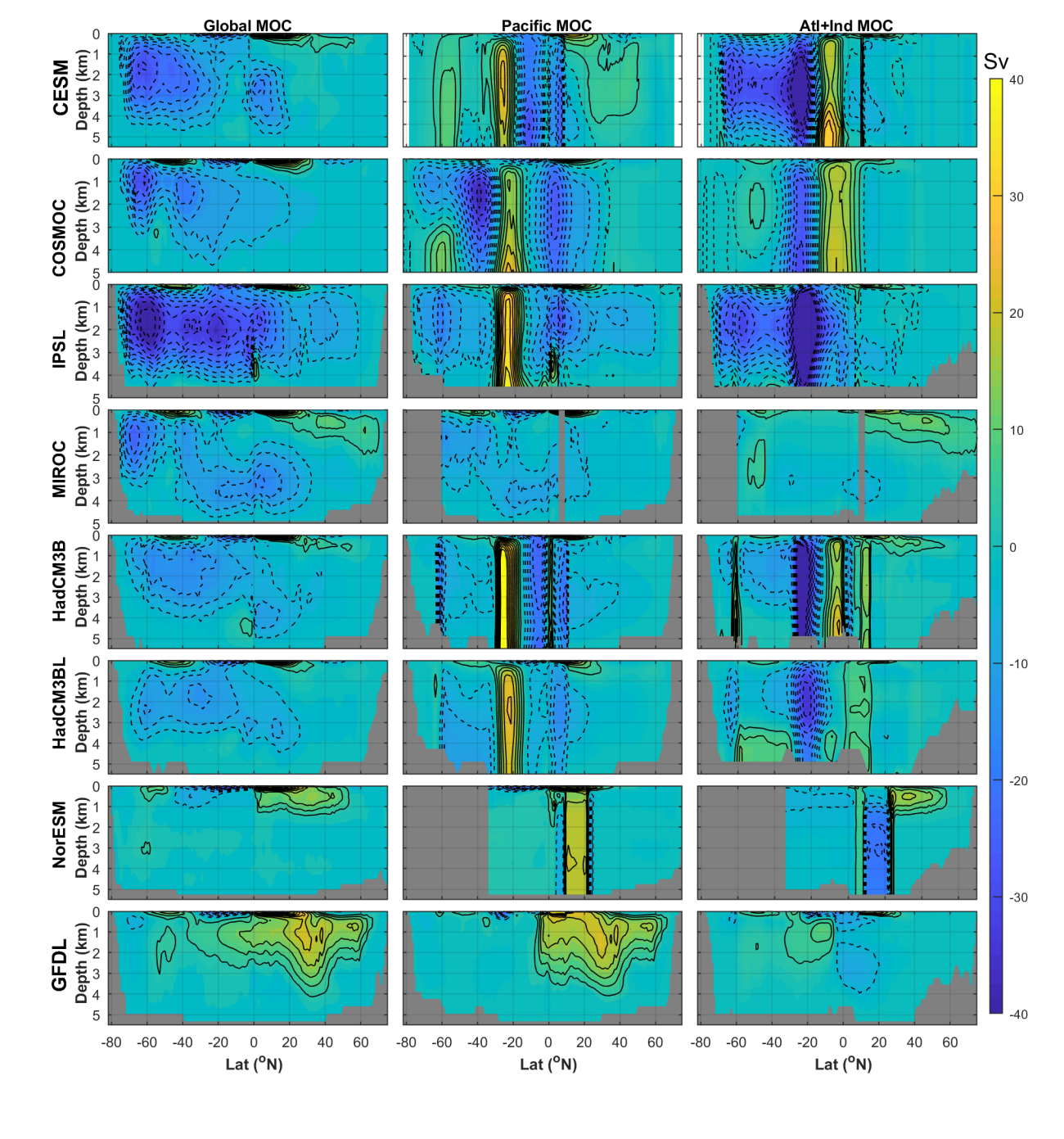


Figure4.

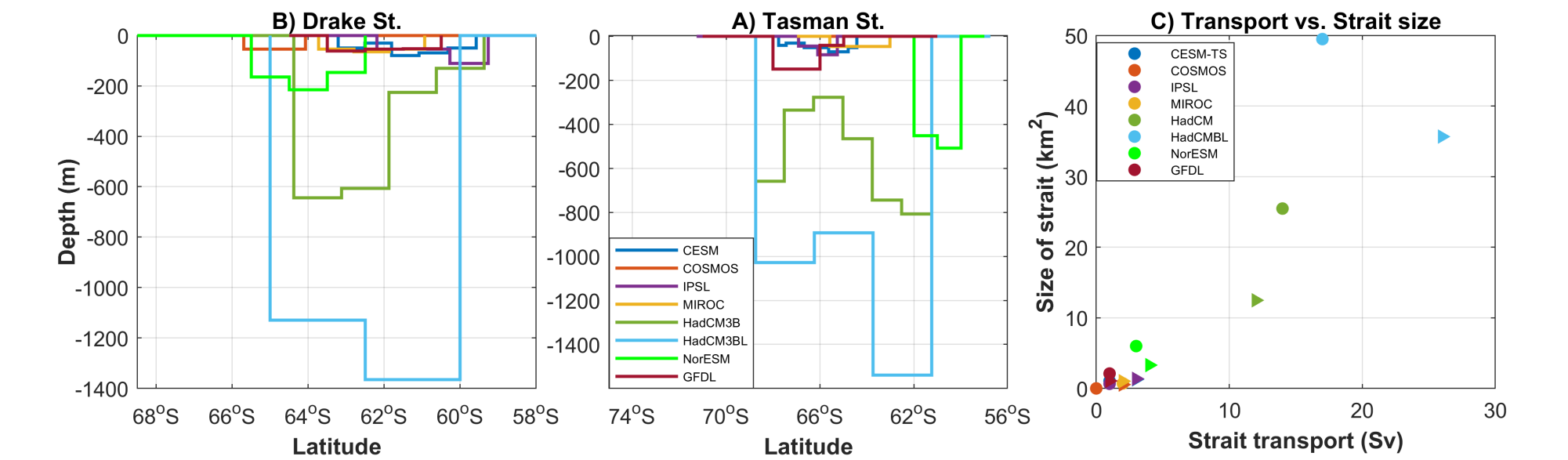


Figure5.			

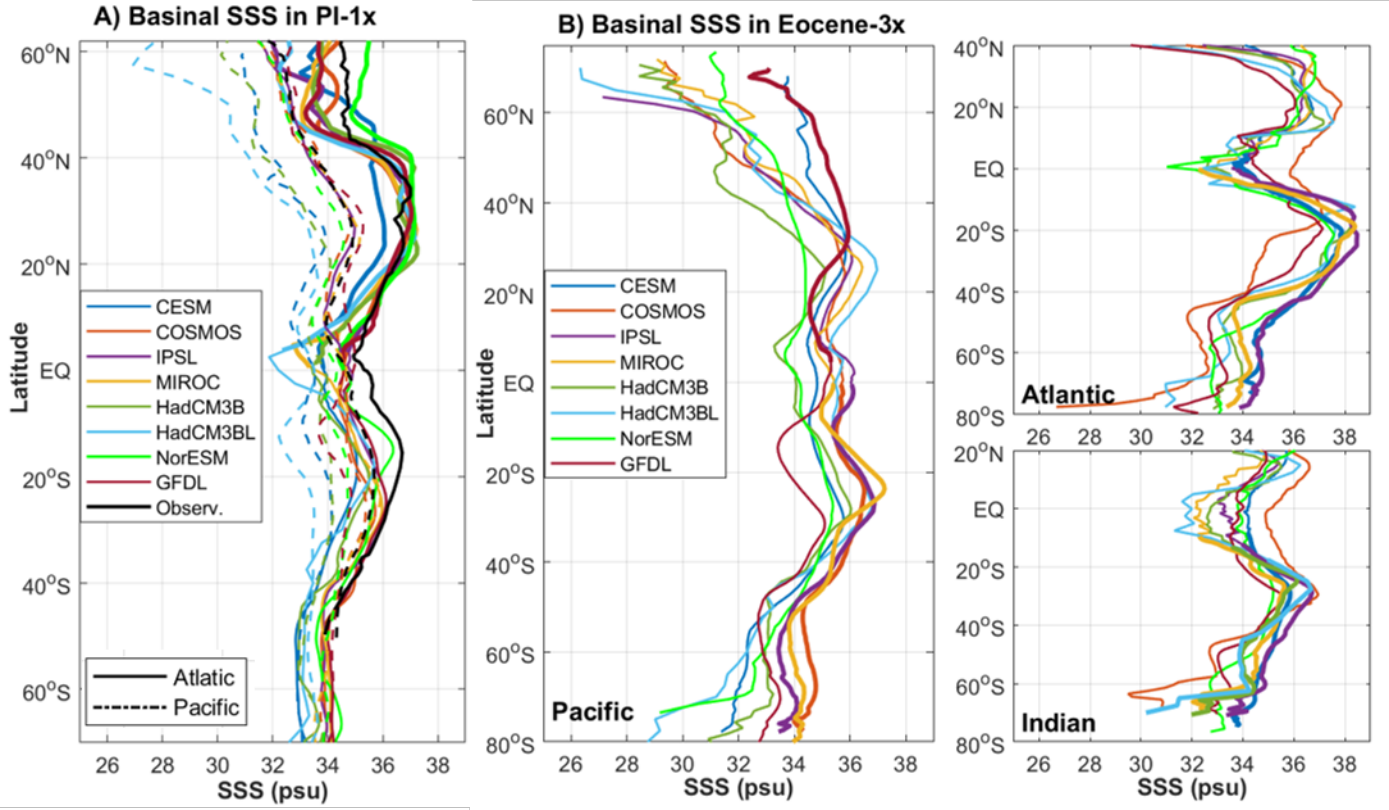


Figure6.		

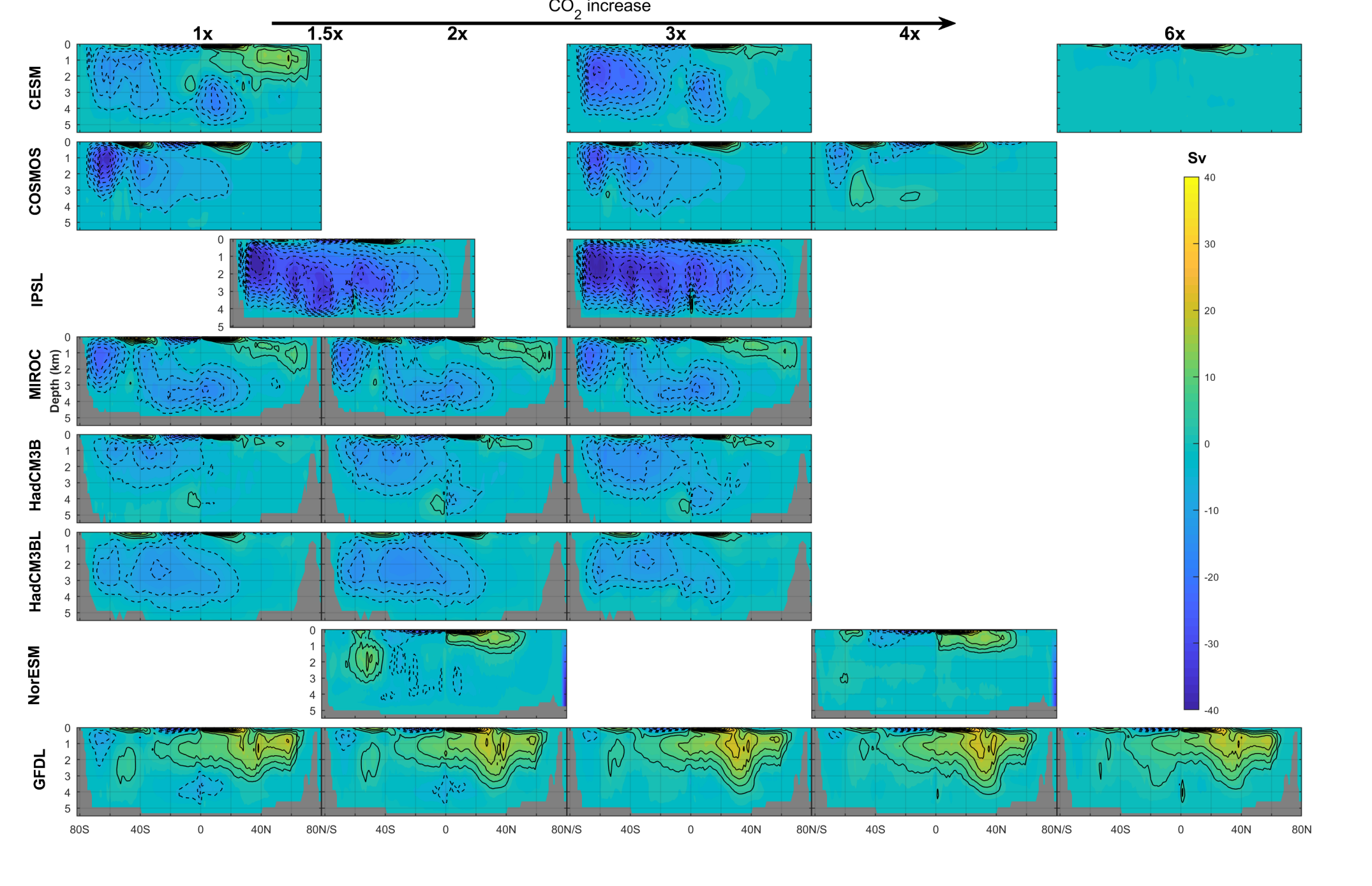
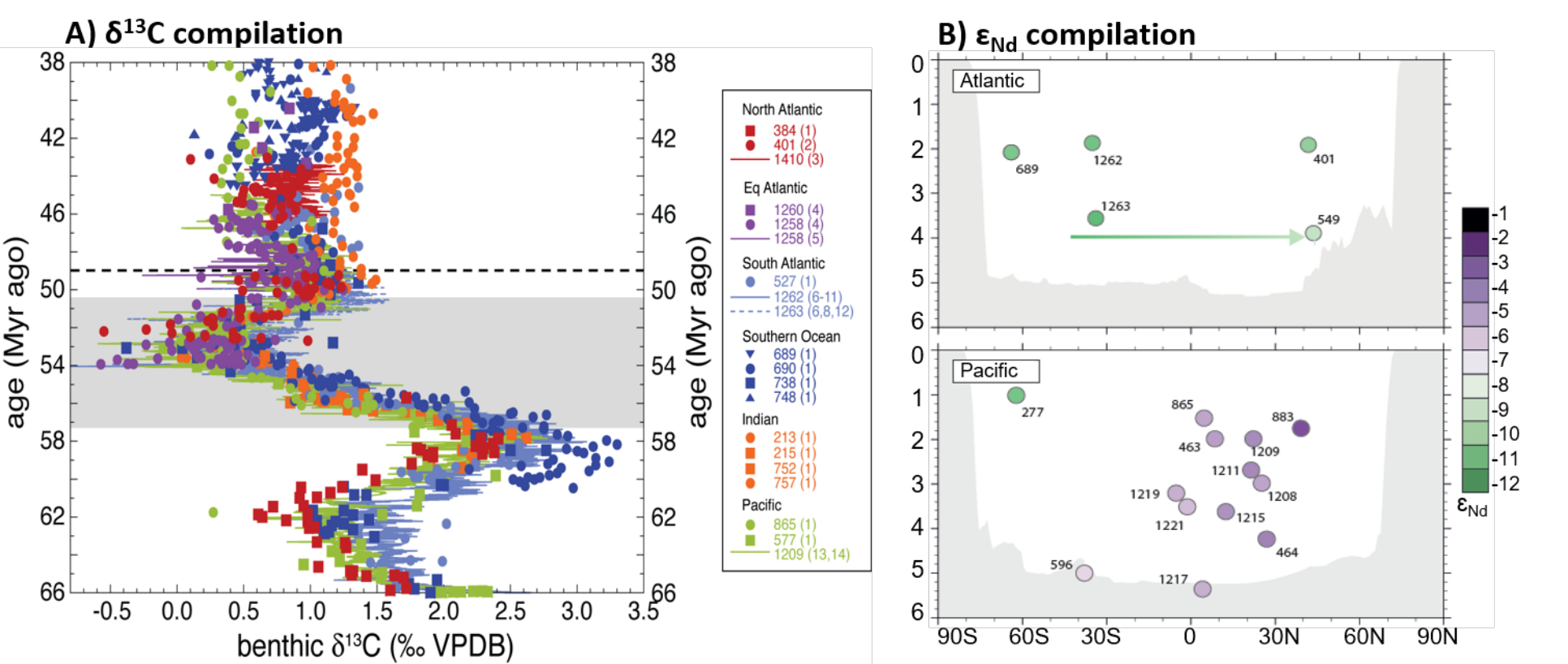


Figure7.	



F	igure8.			

